



NUI Galway  
OÉ Gaillimh

# Resolution Analyses for the Tellus Airborne Electromagnetic Data Compared With Co-located Electrical Resistivity Tomography Data

Somaye Bayat

A thesis presented in fulfilment of the requirements for the  
degree of Masters of Earth and Ocean Sciences

**Supervisors:**

Dr. Duygu Kiyan  
Dr. Eve Daly

School of Natural Sciences  
National University of Ireland – Galway  
Galway City, Ireland  
December, 2022

## Contents

<b>List of Figures</b>	<b>ii</b>
<b>Abstract</b>	<b>v</b>
<b>1 Introduction</b>	<b>1</b>
<b>2 Theory</b>	<b>3</b>
2.1 Basic Principles of Electromagnetic Method . . . . .	3
2.2 Attenuation of Electromagnetic Fields . . . . .	4
2.3 Electromagnetic Properties of Rocks . . . . .	5
2.4 The Airborne Electromagnetic (AEM) Method . . . . .	5
2.4.1 Frequency-domain AEM Systems . . . . .	7
2.4.2 Time-domain AEM Systems . . . . .	8
2.4.3 Acquisition of AEM Data . . . . .	9
<b>3 The Tellus Airborne Electromagnetic Surveys</b>	<b>10</b>
<b>4 Computational Method</b>	<b>12</b>
<b>5 RAFTA Project</b>	<b>16</b>
5.1 Synthetic AEM Data . . . . .	16
5.2 Observed AEM Data and Electrical Resistivity Tomography (ERT) Data .	27
5.2.1 Survey Area . . . . .	27
5.2.2 Tellus FDEM and TDEM Data Inversion . . . . .	27
5.2.3 Electrical Resistivity Tomography (ERT) Data Inversion . . . . .	28
<b>6 Conclusions</b>	<b>38</b>
<b>Bibliography</b>	<b>39</b>
<b>Appendices</b>	<b>40</b>
<b>Appendices</b>	<b>41</b>
A . . . . .	41
B . . . . .	43
B.1 . . . . .	43
B.2 . . . . .	44
C . . . . .	45
D . . . . .	47
E . . . . .	48
F . . . . .	49
G . . . . .	51

## List of Figures

1	The principles of electromagnetic induction in AEM systems . . . . .	4
2	Typical range in electrical conductivity/resistivity for some common mineral rock types and near-surface materials . . . . .	6
3	Frequency-domain EM primary and secondary fields at receiver and Frequency-domain EM response for In-phase and Quadrature of a conductive sphere in AC field . . . . .	7
4	Schematic representation of time-domain EM transmitter and receiver waveforms and time-domain EM response for primary and secondary fields at receiver, for conductivity zones . . . . .	8
5	Schematic illustrations of fixed-wing and helicopter AEM systems . . . . .	9
6	AEM-05 and GENESIS Aircraft used in the Tellus Programme . . . . .	10
7	The Tellus airborne geophysics survey areas . . . . .	11
8	Schematic visualisation of forward and inverse modelling techniques for analysing geophysical data. . . . .	12
9	Structural flowchart of AEMpyx a new version of aempy . . . . .	13
10	Schematic view of a VCP loop configuration over a layered-earth model .	14
11	Tellus survey blocks and boreholes . . . . .	16
12	The workflow followed in this study . . . . .	17
13	Computational forward responses of FDEM and TDEM data from two different three-layer models . . . . .	18
14	The forward responses of the two models calculated at four Tellus survey frequencies different flight altitudes . . . . .	19
15	Computed in-line and vertical components of TDEM data for six different flight altitudes. . . . .	20
16	Tikhonov-type inversion results for a three-layer model at the altitudes of 60 m, 90 m, and 150 m for 100 model samples of FDEM synthetic data. .	21
17	Summary of the output from the Tikhonov-type inversion, which was run for 100 model samples. . . . .	22
18	Tikhonov-type inversion results for a three-layer model at the altitudes of 90 m, 150 m, and 180 m for 100 model samples of TDEM synthetic data. .	23
19	Summary of the output from the Tikhonov-type inversion, which was run for 100 model samples. . . . .	24
20	Tikhonov-type inversion results for a three-layer model at the altitudes of 90 m, 150 m, and 180 m for 100 model samples of TDEM synthetic data. .	25
21	Summary of the output from the Tikhonov-type inversion, which was run for 100 model samples . . . . .	26
22	Bedrock Geology map of the study area . . . . .	27
23	Quaternary Geology (GSI, 1:50,000) map of the study area with the locations of frequency- and time-domain AEM data measurement points and the ERT profiles. . . . .	28
24	Electrical resistivity model from the inversion of Tellus FDEM data . . .	29
25	Electrical resistivity model from the inversion of Tellus TDEM data . . .	30
26	Wenner-Schlumberger array . . . . .	30
27	Electrical resistivity models from the inversion of ERT data using ResIPy software . . . . .	32
28	Electrical resistivity models from the inversion of ERT data using RES2DINV software . . . . .	32
29	Electrical resistivity models from the inversion of Tellus FDEM and TDEM data . . . . .	33

---

---

## LIST OF FIGURES

---

30	Electrical resistivity model from the inversion of the ERT data acquired along the main profile with simulated three-layer resistivity model derived from the ERT resistivity model . . . . .	34
31	1-D Tikhonov-type inversion results of FDEM synthetic data for a three-layer model simulated based on the simplified ERT resistivity model . . . .	36
32	1-D Tikhonov-type inversion results of TDEM synthetic data for a three-layer model simulated based on the simplified ERT resistivity model . . . .	37

## Acknowledgements

I would like to express my deepest appreciation to Dr. Duygu Kiyan, and Dr. Eve Daly for giving me the opportunity to do this research and providing guidance and feedback throughout this project. Special thanks to Dr. Volker Rath for his help and unlimited support in this research and to Dr. Mark Muller for his guidance on the Tellus data. Thanks also to Dave O'Leary and Clodagh Moriarty for their collaborative effort during the ERT survey. I am also grateful to my office mates, Dr. Meysam Rezaeifar for answering my questions tolerantly and Dr. Tao Ye for his help with the QGIS software. Finally, I would like to thank my spouse for supporting me during the compilation of this dissertation. My research would not be possible without the funding from Geological Survey Ireland (GSI) under the GSI Short Call Research Programme 2020 (grant number SC-2020-049).

## **Abstract**

This thesis investigates and compares the capability of frequency- and time-domain air-borne electromagnetic (AEM) data acquired as part of the geophysics surveys of the Tellus programme, which is operated by the Geological Survey Ireland. aempy(x) toolbox written and developed by the Dublin Institute for Advanced Studies researchers is used for forward and inverse modelling of both synthetic and observed Tellus data. As part of the investigation, synthetic data are simulated using two simple three-layer Earth models. The shallow model comprises 15 m thick first layer with a resistivity of 100  $\Omega\text{m}$ , 25 m thick middle layer with a resistivity of 5  $\Omega\text{m}$ , and a lower half-space with a resistivity of 100  $\Omega\text{m}$ , respectively. The deep model comprises 50 m thick first layer with a resistivity of 100  $\Omega\text{m}$ , 50 m thick middle layer with a resistivity of 10  $\Omega\text{m}$ , and a lower half-space with a resistivity of 100  $\Omega\text{m}$ . The inversion process has considered parameters including flight altitude, data errors, and input data, which can have significant effects on the resulting electrical conductivity models. The simulation results show that the simulated frequency-domain data at the flight altitudes of 60 – 120 m have done a much better job recovering the conductive middle layer of the shallow model. On the other hand, time-domain data successfully recovered the first two layers of the second deep model even at high flight altitudes, i.e., 100, 120, and 150 m. The electrical resistivity models derived from the Tellus AEM datasets were compared against the Electrical Resistivity Tomography (ERT) derived resistivity models. The inversion results show that there is a good correspondence between the ERT model and the Tellus TDEM model at greater depths. The Tellus FDEM data successfully resolved the conductivity of the top layer, which is in good agreement with the ERT model.

## 1 Introduction

Airborne Electromagnetic (AEM) systems are specific aircrafts that emit electromagnetic waves to extract information on the Earth's subsurface. AEM was initially developed after the Second World War to explore mineral deposits (Fountain, 1998)<sup>1</sup> and is now one of the most popular geophysical methods used in mineral exploration (Legault, 2015)<sup>2</sup>. AEM geophysics has been increasingly applied to investigate large areas of subsurface due to its time and cost efficiency in producing spatially extensive datasets and its ability to provide high-resolution information about electrical conductivity properties of the shallow subsurface. The electrical conductivity properties of the subsurface depend on various sources such as pore water salinity, clay content, and metallic minerals. AEM data therefore can be used to inform geological and hydrogeological models that can further inform scientific and societal studies.

The Tellus airborne geophysical programme in Ireland, which is operated by Geological Survey Ireland (GSI), started with the first airborne geophysical survey of Northern Ireland, which was flown in 2005 and 2006. It soon was complemented by the Tellus Border project covering five of the six northernmost counties of the Republic of Ireland from 2011 to 2012. In the following years, eleven more surveys were completed, so that, to date, more than 80% of the island of Ireland has been covered. AEM data have been acquired using time-domain and frequency-domain systems.

Under the framework of 2015 GSI Short Call Research Programme, a fully open-source toolbox, *aempy*, coded in Python language for the one-dimensional inversion of AEM data along the flight lines was developed (Kiyan et al., 2022)<sup>3</sup> to make use of the wealth of information on the electrical conductivity structure of Ireland's near-surface provided by the Tellus AEM surveys. GSI is currently producing and making available to the public EM resistivity inversion models computed using the *aempy* code. A number of questions regarding the resolution capabilities of the two Tellus EM systems used, and the resolution of the resistivity models remain, which restricts the confidence with which the models might be interpreted and limits the geological value that might be derived from them. RAFTA (Resolution Analyses for Frequency- and Time-Domain Airborne Electromagnetic Data of the Irish Tellus Programme) project, funded by the 2020 GSI Short Call Research Programme, aims to develop a workflow for uncertainty and resolution analysis of frequency- and time-domain AEM data. The North Midlands survey of the Tellus programme comprises the acquisition of time-domain data, which was carried out by CGG Airborne Survey Ltd. with the GENESIS system. Time-domain data were measured at 11 discrete decay times. All other surveys to date acquired frequency-domain data, which were carried out by Sander Geophysics Ltd. with the GTK airborne system (AEM-95 which operates at 2 frequencies), and the Joint Airborne Geoscience Capability airborne system (AEM-05 operates at 4 frequencies). The North Midlands survey was designed to allow an overlap with the Tellus Border, A1, and A2 survey blocks from which frequency-domain data are available to exploit. As part of the RAFTA project, the aim of this study is to compare the capability of frequency- and time-domain AEM data using synthetic and co-located Tellus frequency- and time-domain AEM datasets from the overlap zone. Additionally, with the aim of investigating how the resistivity structure of the subsurface along the Tellus AEM profiles and how the ground data compare to Tellus AEM inversion data, an Electrical Resistivity Tomography survey was carried out in September 2022 along the 470 m portion of the Tellus AEM profile located in the North Midlands and A1 overlap zone.

The thesis is divided into four sections. Section 2 provides an introduction to the basic theory of AEM method. The two main categories of the AEM method, including frequency- and time-domain systems are presented. The electromagnetic properties of Earth materials are discussed. Section 3 provides information on the Tellus programme

## 1 INTRODUCTION

---

including the aircraft systems used and areas covered as part of the programme. Section 4 briefly describes the computational method used in this study. Section 5 introduces the RAFTA project and discusses the results of forward and inverse modelling of frequency- and time-domain synthetic data and observed Tellus data. This section also compares the resistivity models derived from the AEM data with the inverted ERT models.

## 2 Theory

This section discusses the airborne electromagnetic (AEM) method including the theory, application, acquisition systems, and two main subcategories of AEM systems.

### 2.1 Basic Principles of Electromagnetic Method

Electromagnetic methods are one group of geophysical techniques that estimate subsurface materials' distribution and electromagnetic properties via non-invasive remotely-measured observations. Electromagnetic methods are based on the principle of electromagnetic induction, governed by the famous Maxwell Equations (Maxwell, 1892)<sup>4</sup>, and the fundamental laws of electromagnetism: Faraday's, Ampere's, and Lenz's Laws. The Maxwell equation derivation is collected by four equations, where each equation explains one fact correspondingly. Maxwell combined the four equations by Faraday, Gauss, and Ampere laws and included one part of information into the fourth equation, Ampere's law, which makes the equation complete.

$$\vec{\nabla} \cdot \vec{E} = \frac{\rho}{\epsilon_0} \quad (1)$$

$$\vec{\nabla} \cdot \vec{B} = 0 \quad (2)$$

$$\vec{\nabla} \times \vec{E} = -\frac{\partial \vec{B}}{\partial t} \quad (3)$$

$$\vec{\nabla} \times \vec{B} = \mu_0 \left( \epsilon_0 \frac{\partial \vec{E}}{\partial t} + \vec{J} \right) \quad (4)$$

Equation 1 and 2 represent Gauss law intended for static electric fields and static magnetic fields respectively. Faraday's Law (Eq. 3) explains that the change of magnetic field will produce an electric field, and Equation 4 is Ampere-Maxwell's law, which relates the change of electric field which produces a magnetic field. In these equations, ( $E$ ) denotes electrical field, ( $\epsilon_0$ ) denotes permittivity, ( $j$ ) denotes current density, ( $\mu_0$ ) is permeability, and ( $c$ ) is the speed of light. Faraday's and Lenz's laws state that the electromotive force, e.m.f, induced in a circuit is equal to the negative rate of change with time of the magnetic flux through the circuit given as:

$$\oint E \cdot dl = -\frac{d\phi}{dt} \quad (5)$$

Where  $\oint E \cdot dl$  is the line integral of the induced electric field ( $E$ ) around the wire coil and  $\frac{d\phi}{dt}$  is the rate of change of magnetic flux through the circuit. Ampere's Law states that the line integral of the magnetic field around a closed loop is proportional to the electric current flowing through the loop; that is, it relates the magnetic field to a current loop (Grant and Phillips, 1990)<sup>5</sup>. Maxwell related Faraday's law, Ampere's law, and Gauss's law into a single unifying theory of electromagnetism. Thus, the current loop, the electromagnetic fields, the subsurface electromagnetic properties, and the voltages measured in the receiver coils are all governed by solving Maxwell's equations (Maxwell, 1892)<sup>4</sup>. The principle of electromagnetic induction is shown in Figure 1.

The system involves the transmission of electromagnetic energy via a wire loop carrying a time dash varying current that has associated magnetic and electric fields. These primary fields create eddy currents associated with secondary magnetic and electric fields, flowing in the subsurface material with different conductivity. Since the electromagnetic properties of the subsurface influence the induced subsurface currents and their associated secondary fields, analysis of the detected fields enables inferences about the subsurface

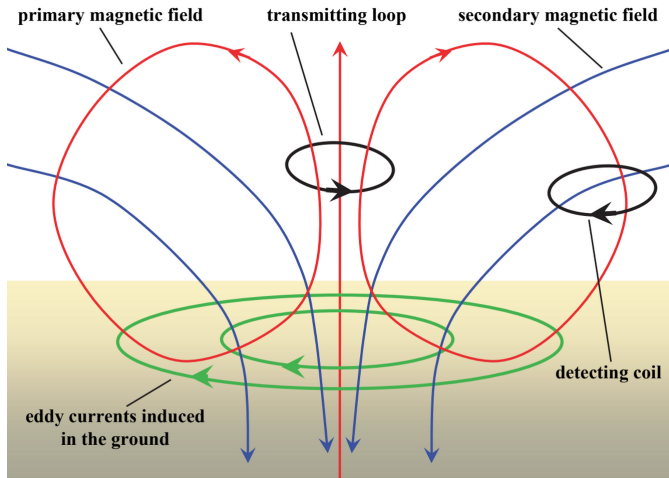


Figure 1: The principles of electromagnetic induction in AEM systems. Above the ground, a time-varying sinusoidal current is driven through a wire loop, causing eddy currents to flow in the subsurface. The eddy currents have an associated, secondary varying magnetic field. This secondary field is then detected at the specific receiver coil as a voltage which can be examined to extract valuable information on the conductivity of the subsurface (Brodie, 2017)<sup>6</sup>.

materials. Knowledge of the electromagnetic properties of subsurface materials, the electrical conductivity ( $\sigma$ ), the magnetic permeability ( $\mu$ ), and the dielectric permittivity ( $\epsilon$ ), has significance in geoscience, environmental science, and geotechnical sciences.

## 2.2 Attenuation of Electromagnetic Fields

An important characteristic of the time-varying electromagnetic field is its attenuation with distance through a conductive medium. Attenuation is a consequence of energy lost by the circulating eddy currents and their magnetic fields. For a sinusoidally varying field in an infinite uniform conductive medium, and where the effect of the dielectric property is very small compared with the effect of conductivity, the skin effect is quantified in terms of a parameter known as skin depth ( $\delta$ ). Skin depth is the distance over which the electromagnetic field's amplitude is attenuated by  $1/e$  (i.e., 37%) of its surface value and is given by:

$$\delta = \frac{1}{\sqrt{\pi\mu\sigma f}} \quad (6)$$

where  $\mu$  is the magnetic permeability of a homogenous medium in Henry/m,  $\sigma$  is electrical conductivity in Siemens/m,  $f$  is the frequency in Hertz and the skin depth is in the meters. The magnetic permeability of most rocks is nearly the same as that in a vacuum ( $\mu = \mu_0 = 4\pi \times 10^{-7}$ ) (Zhdanov and Keller, 1994)<sup>7</sup> allowing the expression to be written as:

$$\delta = \frac{503.8}{\sqrt{\sigma f}} \quad (7)$$

This value is not the limiting distance or the depth of the field's penetration, but a convenient measure of the attenuation in terms of distance or depth. The equation shows that EM fields attenuate faster in materials of high conductivity and the attenuation is greater for fields of higher frequency. In the time-domain a measure of skin depth which is known as the diffusion depth is the depth to the maximum current density at a particular

delay time ( $t$ ) and depends on the electrical conductivity ( $\sigma$ ) and magnetic permeability ( $\mu$ ). It is given by the expression:

$$d = \sqrt{\frac{2t}{\mu\sigma}} \quad (8)$$

Where  $t$  is in seconds,  $d$  in meters, and  $\sigma$  in Simens/metre. The expression is written as:

$$d = 1261.6 \sqrt{\frac{t}{\sigma}} \quad (9)$$

Diffusion depth is larger for the more resistive ground because the current system diffuses faster into it. A receiver at the surface senses the smoke ring attenuating quickly, i.e., a rapid decay in signal amplitude as the distance to the moving smoke ring rapidly increases. In the resistive ground, it is necessary to make measurements at early delay times in order to detect the rapidly expanding smoke ring. Its velocity decreases with increasing conductivity; in other words, diffusion is a slow process in the conductive ground. As a consequence, measurements made at early delay times pertain to shallower depths in conductive environments than in resistive ones. Note that without the conductivity being known, the delay time is an unreliable indicator of the depth to which particular measurements pertain.

### 2.3 Electromagnetic Properties of Rocks

Three physical properties of rocks which affect the propagation of the electromagnetic are electrical conductivity ( $\sigma$ , S/m), magnetic permeability ( $\mu$ , H/m), and dielectric permittivity ( $\epsilon$ , F/m). The dielectric constant is defined as material's ability to be electrically polarised and has an important control of the responses of high-frequency EM surveys (Qifei and Manika, 2016)<sup>8</sup>. Magnetic permeability is a value that expresses how a magnetic material responds to an applied magnetic field. Magnetic permeability is related to the more fundamental property, magnetic susceptibility  $K_\mu$  through the expression:

$$\mu = \mu_0(1 + K_\mu) \quad (10)$$

Where  $\mu_0 = 4\pi \times 10^{-7}$  (H/m) is the magnetic permeability of free space. Electrical conductivity is a measurement of how easily a material allows electric current to flow through it. Inversely, electrical resistivity measures how strongly a material resists the flow of electric current ( $\sigma = \frac{1}{\rho}$ ). Electrical conductivity is the most important and practical electromagnetic property estimated from AEM data. Figure 2 is a diagram that shows the typical range of conductivity of common earth materials.

Base metal sulphides are typically very conductive and are important targets in mineral exploration applications. Native metals and graphite are also conductive rock constituents. Almost all other rock-forming minerals act as insulators. There are exceptions for some clay minerals that serve to increase conductivity via ion exchange processes if they are wet (Keller, 1988)<sup>9</sup>. This is an important factor in the AEM mapping of the Regolith zone. The electrical conductivity/resistivity of a rock depends significantly on its mineralogy and pore-water properties.

### 2.4 The Airborne Electromagnetic (AEM) Method

There are several operating systems for electromagnetic methods based on attributes like dimensions, orientation, and spectral content of the transmitting source, the relative position and direction of the transmitter and receiver, how the receiver detects the fields, and how a survey is carried out. This thesis works with the airborne electromagnetic method,

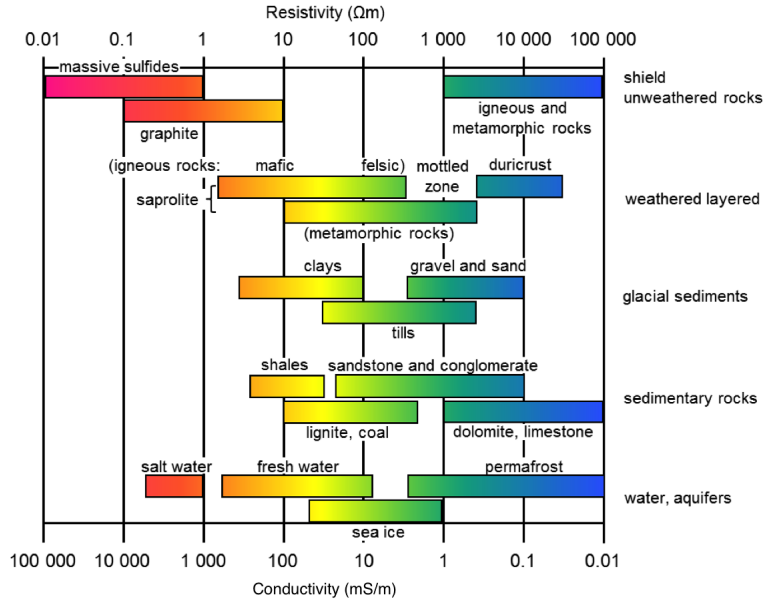


Figure 2: Typical range in conductivity/resistivity for some common mineral rock types and near-surface materials (modified from Palacky, 1993)<sup>10</sup>.

a class of electromagnetic in which an aircraft carries or tows the transmitting and receiving instrumentation through the air. AEM geophysics has been increasingly applied to investigate large subsurface areas due to its time and cost efficiency in producing spatially extensive datasets and its ability to provide high-resolution information about the electrical conductivity properties of the shallow subsurface. Two main subcategories of AEM systems are frequency-domain (FDEM) and time-domain (TDEM) systems. Both methods are explained in detail in the following sub-sections. However, in summary, FDEM systems transmit a continuous sinusoidal current waveform through multiple loops at different discrete frequencies. In contrast, TDEM systems transmit a pulsed (i.e., on then off) current waveform through one loop. AEM systems were developed in the frequency-domain in Canada in 1946 (Palacky and West, 1991)<sup>11</sup> to detect the conductive massive sulphide bodies within the resistive rocks of the Precambrian shield. The following need to explore other types of targets and the different kinds of geological environments combined with the development in EM systems has led to higher sensitivity of time-domain systems, which are now being used almost exclusively for mineral exploration and geological mapping. In particular, TDEM systems have superior performance in areas of conductive overburden compared with FDEM systems; they can detect good conductors located at a significant depth below conductive overburden. FDEM systems now find application mainly to shallower groundwater and environmental studies (Dentith and Mudge, 2014)<sup>12</sup>. AEM surveys aim to improve our information about the subsurface by acquiring knowledge of its electromagnetic properties. Its application is considerable, where there is sufficient contrast between the electromagnetic properties of the various subsurface units. In these units, the electromagnetic properties can act as a representative parameter for subsurface mapping. The bulk electromagnetic properties of rocks are a complex function of multiple variables (e.g., mineral content, porosity, pore fluid conductivity, and saturation), so this method is not practical for determining the composition of mineral ores or lithological units.

Although AEM method was originally developed as a mineral exploration tool, including the detection of massive sulphides, unconformity-style uranium mineralization, Kimberlites, and mapping of Palaeochannels as a potential host for placer deposits and sandstone-

hosted uranium deposits, it is becoming more common in geological mapping to complement magnetic and gravity surveys, mapping groundwater to detect water resources and water quality characterisation (Sengpiel, 1983<sup>13</sup>; Fitterman and Deszcz-Pan, 1998<sup>14</sup>; Sattel and Kgolihang, 2004<sup>15</sup>; Auken et al., 2007<sup>16</sup>) and Soil salinity (Anderson et al., 1993<sup>17</sup>; Street et al., 1998<sup>18</sup>; Lawrie et al., 2000a<sup>19</sup>; Brodie et al., 2004b<sup>20</sup>)

#### 2.4.1 Frequency-domain AEM Systems

In the frequency-domain systems, a continuous sinusoidal (a.c.) current produces a primary magnetic field, usually at several frequencies. The primary magnetic field induces sinusoidally varying eddy currents into a conductor (Fig. 3A). They circulate in the conductor and are out of the phase with respect to the primary field. Properties of the conductor affect the strength and phase of eddy currents so by measuring these properties, information can be obtained about the subsurface conductivity (Dentith and Mudge, 2014)<sup>12</sup>.

The FDEM systems consist of multiple coil sets that consist of a transmitter (Tx) and a receiver (Rx). The transmitter consists of a wire coil through which a continuous sinusoidal current is passed at a single fixed discrete frequency. This time-varying, alternating current (a.c.) is related to an alternating primary magnetic field by Ampere's law. By Faraday's and Lenz's laws, this magnetic field propagates from the transmitter and induces eddy currents to flow in the electrically conductive subsurface material. A secondary field, which is influenced by the various conductive properties of the earth's subsurface geology, is then produced and measured by the receiver. In each receiver, there is one coil tuned to receive at the specific frequency of its paired transmitter. Analysis of the voltages measured in the receiver coils allows inferences about the subsurface materials' electromagnetic properties. The total magnetic field that will be measured at the ( $R_x$ ) is

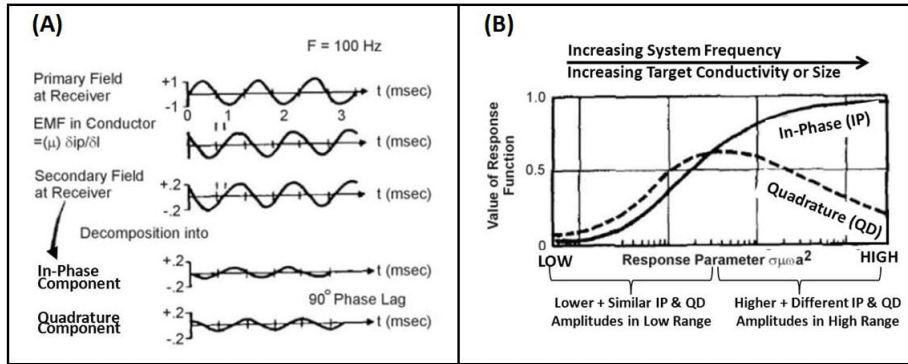


Figure 3: (A) Frequency-domain EM primary and secondary fields at receiver. (B) Frequency-domain EM response for In-phase and Quadrature of a conductive sphere in AC field (after Klein and Lajoie, 1980)<sup>21</sup>.

the sum of the primary ( $B_p$ ) and secondary ( $B_s$ ) magnetic fields (Fig. 3). FDEM response is defined as the secondary magnetic field ( $B_s$ ) normalised by the primary magnetic field ( $B_p = B_0$ ). FDEM separates the secondary fields from the primary by subtracting the difference between the measured and predicted fields, with FDEM data expressed as in-phase (real) and quadrature ( $90^\circ$  out of phase/imaginary) components (Legault, 2015)<sup>2</sup>:

$$I = \frac{R(B_{tot})}{B_0} - 1 \quad Q = \frac{Im(B_{tot})}{B_0} \quad (11)$$

where  $R(B_{tot})$  is the component of the total field that is in the same phase as the primary field and  $Im(B_{tot})$  is the component that has a  $90^\circ$  phase shift with the primary field. AEM data are presented in units of parts per million (ppm) (Kiyan and Rath, 2017)<sup>22</sup>.

### 2.4.2 Time-domain AEM Systems

In time-domain systems, change in the primary magnetic field is produced by either abruptly turning-off or turning-on a steady (d.c.) current (Fig. 4A). A pulse of current is induced in a conductor, causing the circulation of eddy currents in the conductor for a short period and quickly decay as they lose energy. Monitoring their decay provides information about the subsurface conductivity because their strength and duration are dependent on the electrical characteristics and geometry of the conductor (Fig. 4B). The delay time refers to the strength of the secondary magnetic field as a function of time, since the primary field turn-off or on. Channels are measurements for a specific delay time, and they are frequently identified by their numbers, for example, channel 1 refers to the least delay time. Generally, the measurements are recorded after the pulse turn-off, where there is no primary field, and are known as the off-time measurements.

Accurate time synchronisation for transmitter and receiver is crucial since measurements are made at millisecond intervals with time series typically spanning a few tens of milliseconds and spanning a few seconds when measuring very slow decays. Although each measurement is nominally made at a defined delay time, in practice, most EM systems make a very large number of measurements of the secondary decay for tens to thousands of repetitions of the transmitted pulse. Multiple decay measurements enable equivalent measurements in the time series to be stacked to reduce noise. This is particularly important at late delay times when the secondary signal is very weak and usually obscured by noise. The stacked measurements are merged into a smaller number of receiver ‘windows,’ also referred to as channels, which have a finite time-width that increases with delay time. The channel amplitudes form the final representation of the decaying secondary field.

The time spacing between the channels is approximately logarithmically spaced. In order to accurately record this rapidly changing part of the decay, more closely timed channels are required than they are for the more slowly changing late-time decay. The delay time for each channel and the period over which the decay is recorded are set by the system base frequency. On-time measurements are critically affected by variations in the location of the receiver with respect to the transmitter, which causes variation in the measurements. Accurate monitoring of system geometry is essential in order to minimise this system noise. TDEM measurements are made when the primary field is turn-off, so the receiver sensitivity is maximised to detect the weaker secondary signals, and variation in the orientation and location of the receiver with respect to the transmitter are not a source of the noise (Dentith and Mudge, 2014)<sup>12</sup>.

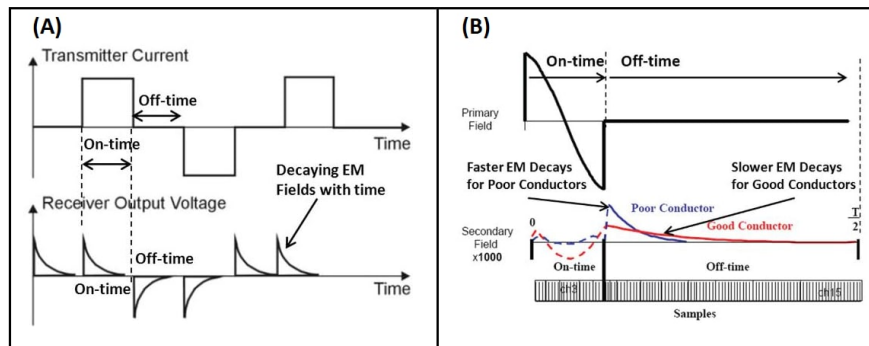


Figure 4: (A) Schematic representation of time-domain EM transmitter and receiver waveforms (after US EPA Environmental Geophysics website). (B) Time-domain EM response for primary and secondary fields at receiver, for a low (Poor=Blue) and high (Good=Red) conductivity zones (after Allard, 2007)<sup>23</sup>.

### 2.4.3 Acquisition of AEM Data

Although there are some obvious distinctions, AEM systems perform similarly to ground EM systems. AEM systems carry both the transmitter and the receiver on the moving platform. The transmitter loop is located at a height above the ground, so the induced eddy current is laterally more expansive and locally weaker than the same loop of the ground surface system. In addition, the loop is smaller than that typically used in ground systems, the transmitter and receiver are further from the target, and the measurement is naturally noisier, so more attention is required to maximize the signal-to-noise ratio in both the instrumentation and the data reduction. AEM systems generally have a more powerful transmitter than ground systems. Two main categories of AEM systems are towed-bird fixed-wing and rigid-frame helicopter systems (Fig. 5). Both categories have several special systems and response characteristics in common. The primary determinants of system selection are the operational characteristics of each class of aircraft, i.e., fixed-wing aircraft for wide-area regional surveying and helicopters for local-area low-level surveying (Dentith and Mudge, 2014)<sup>12</sup>.

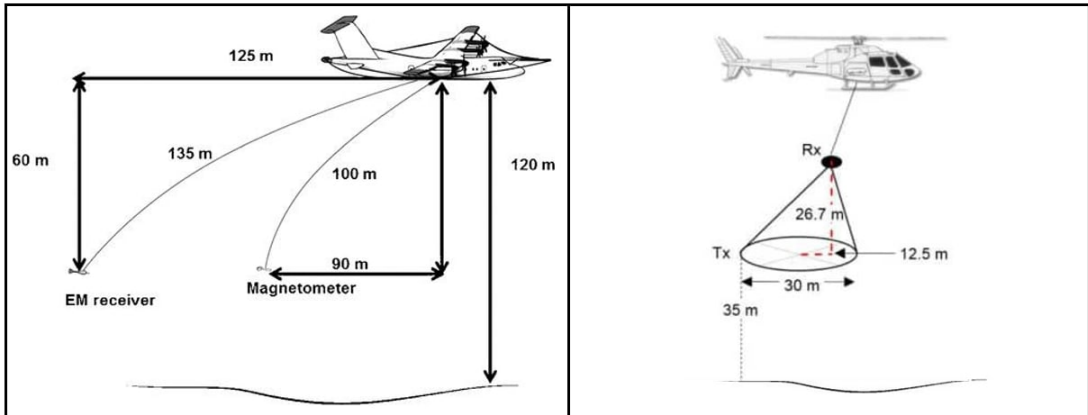


Figure 5: Schematic illustrations of fixed-wing (left) and helicopter (right) AEM systems (modified from Dentith and Mudge, 2014)<sup>12</sup>.

### 3 The Tellus Airborne Electromagnetic Surveys

Tellus is a national programme managed by Geological Survey Ireland (GSI) and funded by the Department of the Environment, Climate and Communications (DECC), aimed at collecting geophysical and geochemical data across Ireland to support environmental and natural resource management. The Tellus airborne geophysical survey collects magnetic, electromagnetic (EM), and radiometric (gamma-ray spectrometry) from a low-flying, all-metal, fixed-wing, aircraft.

The Northern Ireland part of the Tellus Programme was carried out with the GTK AEM-95 system which had two frequencies (3125 and 14368 Hz). The other FDEM surveys were completed using the improved AEM-05 system which was developed as Joint Airborne Geoscience Capability (JAC) by a partnership between the Finnish and British Geological Surveys. The AEM-05 system operates at four frequencies, 912 Hz, 3005 Hz, 11962 Hz, and 24510 Hz, and is subsequently operated by Sanders Geophysics Ltd. Orthogonal in-phase and quadrature components of the EM responses at each frequency are recorded and subsequently processed independently of each other, providing eight components of data at each measurement location (Muller and Hodgson, 2020)<sup>24</sup>. The nominal flight speed of 60 m/s and 10 Hz EM data sampling rate provides measurement locations at approximately 6 m intervals along the flight lines. The transmitter and receiver coils are mounted on separate wings (Fig. 6A) in a vertical-coplanar orientation with a coil separation of approximately 21.4 m. The system is also equipped with a 50/60 Hz power line monitor, which becomes particularly useful in identifying cultural interference when surveying in urban settings (Ture et al., 2017)<sup>25</sup>. The survey altitude in rural areas is 60 m and 240 m in urban areas (Hodgson and Young, 2016)<sup>26</sup>.

Tellus North Midland (TNM) survey was carried out with the CGG GENESIS system. The GENESIS 3-axis towed bird assembly provides accurate low noise sampling of the X (horizontal in line), Y (horizontal transverse), and Z (vertical) components of the electromagnetic field. The receiver coils measure the time derivative of the magnetic field (dB/dt). Signals from each axis are transferred to the aircraft through a tow cable specifically designed for its electrical and mechanical properties. The EM transmitter (TX) was mounted above the aircraft with a loop running between the wings and tail mount. The EM receiver (RX) was deployed on a bird 45 m below the aircraft (Fig. 6B). Only X and Z data collected were processed and delivered. A nominal flight altitude of 90 m above the ground level was used for the TDEM data acquisition at eleven Tellus time windows for both  $B_{\text{inline}}$  and  $B_{\text{vertical}}$  components.

Figure 7 shows a map of the areas completed by the Tellus programme from 2005 to 2021. Close to 80% of Ireland have been surveyed by 2021. More details of the areas completed through the Tellus's AEM surveys can be found in Table 1.

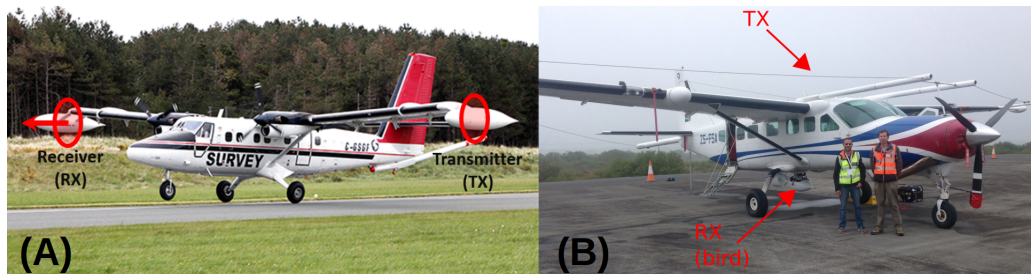


Figure 6: (A) Airplane operated by SGL for the FDEM surveys. (B) Airplane operated by CGG for the TDEM survey in the Northern Midlands between September 2013 and Jun 2015.

### 3 THE TELLUS AIRBORNE ELECTROMAGNETIC SURVEYS

---

Table 1: State of the Tellus AEM survey as of May 2022.

Block	system	Date / site
NI	AEM-05	2005-2006 / Tellus Northern Ireland
	AEM-95	
TB	AEM-05	2012 / Tellus Border
TNM	GENESIS	2014-2015 / North Midlands
WFD	AEM-05	2016 / County of Waterford
A1	AEM-05	2016 / East of the Country
A2	AEM-05	2016-2017 / County Galway
A3	AEM-05	2017-2018 / County Mayo
A4	AEM-05	2017-2018 / County Donegal
A5	AEM-05	2018-2019 / Limerick
A6	AEM-05	2018-2019 / West Cork
A7	AEM-05	2019 / South East Ireland
A8	AEM-05	2020 / Dunmore East
A9	AEM-05	2021 / County Cork

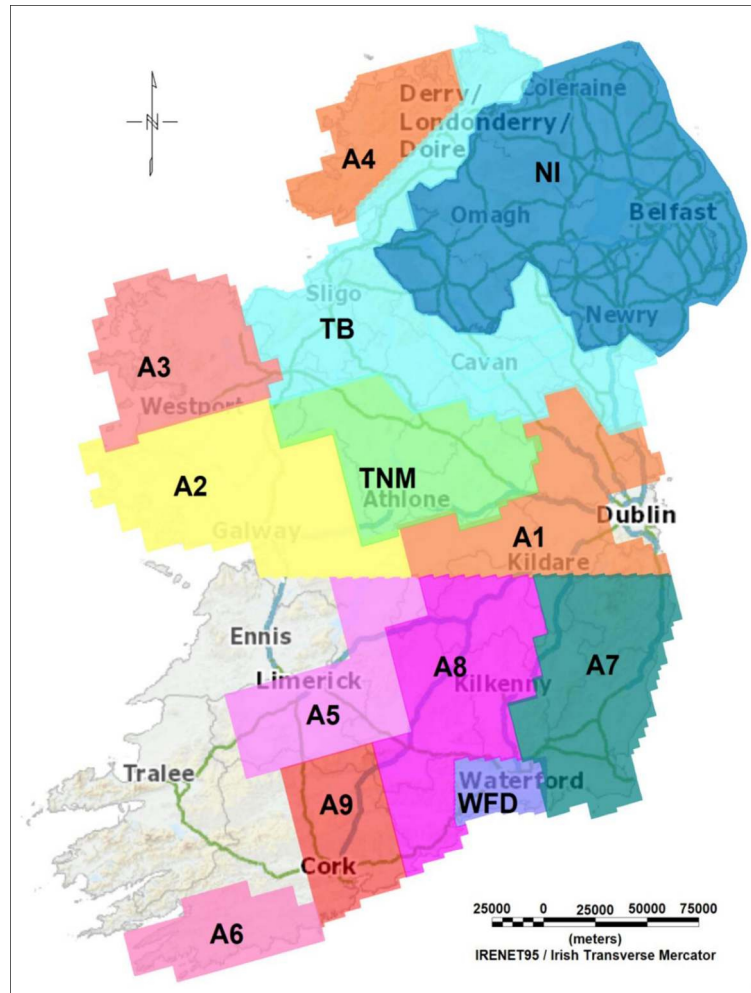


Figure 7: The Tellus airborne geophysics survey areas. The coloured polygons show the counties investigated between 2005 and 2021. Provided by GSI.

## 4 Computational Method

There are two different modelling techniques for analysing geophysical data: forward and inverse modelling. Forward modelling is the process of predicting data when the model of the earth is known. The inversion modelling, or inversion, is a data-fitting, optimisation approach and finds the ‘best’ model according to a given criterion, which leads to one preferred model (Kiyan and Rath, 2022 and references therein)<sup>3</sup>. A simplified description of inverse modelling together with forward modelling is presented in Figure 8.

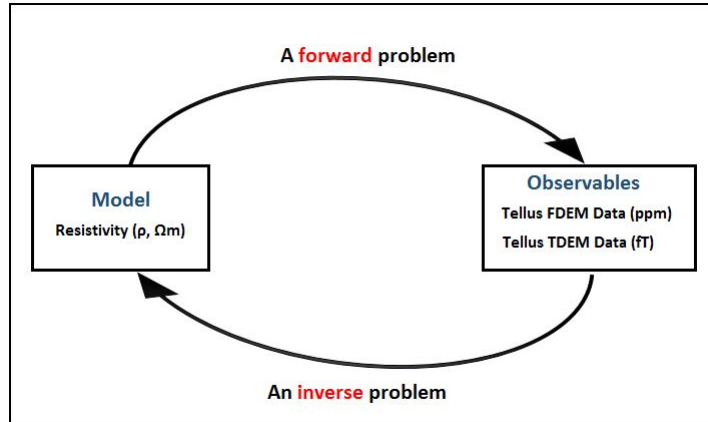


Figure 8: Schematic visualisation of forward and inverse modelling techniques for analysing geophysical data. Forward modelling is the process of predicting data when the model of the earth is known. The inversion modelling or inversion is a data-fitting, optimisation approach and finds the ‘best’ model according to a given criterion, which leads to one preferred model.

Inverse modelling requires the user to specify a starting model which is systematically refined by the inversion process. The task for the inversion is to adjust model parameters so as to minimise the difference between the observed and the calculated responses at each data point.

In this study, forward and inverse modelling of the AEM data was accomplished using the extended version of aempy suite of software tools. aempy is an open source, Python based EM processing and modelling “toolbox” developed by researchers at Dublin Institute for Advanced Studies, funded by a GSI Short Call Research Award in 2015 (Kiyan and Rath, 2017)<sup>22</sup>, (Kiyan et al., 2022)<sup>3</sup>. Since the original aempy implementation, the toolbox has been migrated from Python 2.7 to 3.7+ (currently being developed under 3.9). The extended version of the aempy toolbox is called aempyx, which has been developed and implemented in project RAFTA (Resolution Analyses for Frequency- and Time-Domain Airborne Electromagnetic Data of the Irish Tellus Programme) funded by GSI Short Call Research Award in 2020.

The aempy toolbox (Kiyan and Rath, 2017)<sup>22</sup> and (Kiyan et al., 2022)<sup>3</sup> is an open-source, flexible package of software providing capacity for the 1-D inversion of frequency- and time-domain AEM data. The software is written in the Python language and calls on several numerical packages in Python, namely numpy, scipy and matplotlib. Capacities of the toolbox are implemented in several high-level scripts that cover a full workflow from (i) loading and reformatting of raw AEM data, (ii) pre-processing of EM responses, (iii) inverse modelling, and (iv) visualisation of outputs.

- (i) Data management tools include reformatting raw EM data to an internal aempy format, data subset selection based on polygons or rectangles, projection of data onto a new profile, and various graphical visualisations of the input data.

## 4 COMPUTATIONAL METHOD

---

(ii) EM data pre-processing functions include the masking of non-physical data (e.g., flagging, deleting, or interpolating measurement sites in high-fly zones or in the vicinity of man-made installations), several interpolation approaches (i.e., moving average and median window) and Principal Component Analysis (PCA) to improve the spatial consistency of the inversion results.

(iii) Implementation of several 1-D EM inversion approaches:

- Tikhonov-type regularised inversion (Used in the thesis)
- Bayesian MAP (maximum a posteriori probability) inversion in parameter and data space. (Not used in the thesis)
- Full Bayesian Markov Chain Monte Carlo (MCMC) inversion. (Not used for the thesis)

(iv) Various graphical visualisations of input and filtered EM responses, observed and predicted EM responses (post-inversion), and resistivity model cross-sections.

The inversion workflow implemented in aempyx is summarised in Figure 9 and consists of three main components. The computational core of the Tikhonov-type 1-D layered

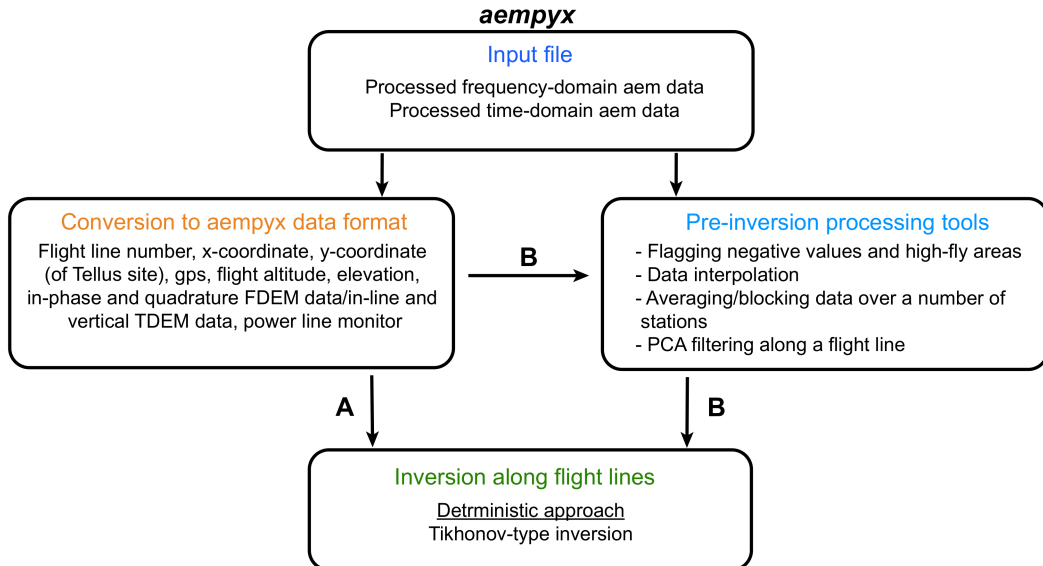


Figure 9: Structural flowchart showing the aempyx features used in this study (modified from Kiyan et al., 2022)<sup>3</sup>. A: processed AEM data can be directly inverted. B: the user can use pre-inversion processing tools prior to performing inversions.

inversion is based on an adapted forward modeller taken from the well-tested, open source AirBeo code. This code was originally developed by Australia's CSIRO and the AMIRA consortium (Raiche et al., 2017). The inversion code in aempy is customised for the physical configuration of the Tellus airborne EM systems:

- (i) The AEM-05 system, which operates at four frequencies (24510 Hz, 11962 Hz, 3005 Hz, and 912 Hz), with vertical, co-planar transmitter and receiver coils (VCP or CpX configuration) mounted at the tips of the aircraft wings with fixed coil separations of 21.35 m for 912 and 3,005 Hz and 21.38 m for 11,962 and 24,510 Hz.
- (ii) The GENESIS system, which operates at eleven time channels. It is essentially a TEMPEST system, adapted to shallow surveys. The GENESIS 3-axis towed bird assembly provides accurate low noise sampling of the X (horizontal in line), Y (horizontal transverse), and Z (vertical) components of the electromagnetic field.

The 1-D (layered) forward model assigns seven physical properties to each layer  $n$ , including its thickness of  $\delta Z_n = thK_n$ . The layer physical parameters are the electrical resistivity  $\rho_n$ , dielectric permittivity  $\varepsilon_{r,n}\varepsilon_0$ , magnetic permeability  $\mu_n = \mu_{r,n}\mu_0$ , chargeability  $m_n$ , time constant  $t_n$  and frequency constant  $c_n$ . Here  $\varepsilon_0 (8.85 \times 10^{12} F/m)$  and  $\mu_0 (4\pi \times 10^7 H/m)$  are the dielectric permittivity and magnetic permeability of the free space, respectively.  $r$  denotes the relative value used for the parameterization in the respective layer. Parameters chargeability, time constant, and frequency constant are the so-called Cole-Cole parameters (Cole and Cole, 1941)<sup>27</sup> and are kept constant in this study. Figure 10 presents the schematic view of a VCP loop configuration over a layered earth model. The AEM response is positioned at the centre between the Transmitter (TX) and Receiver (RX). The spacing ( $r$ ) between them is constant. For the Tellus FDEM Surveys,  $r \approx 21.4$  m. The survey design parameters for the FDEM data acquisition in Ireland are: a nominal flight altitude of 60 above ground level and flight lines with a fixed orientation of 345° (NNW-SSE), (perpendicular to the most common lithological and structural trends in Ireland), and a 200 m lateral spacing. The FDEM system, AEM-05 system, operates at four frequencies, (912 Hz, 3005 Hz, 11,962 Hz, and 24,510 Hz). A nominal flight altitude of 90 m above ground level was used for the TDEM data acquisition at eleven Tellus time windows for each component,  $B_{\text{inline}}$  and  $B_{\text{vertical}}$ .

The synthetic and observed Tellus AEM data were inverted for a single parameter only, electrical resistivity, using fixed layer thicknesses and depths for all sites.

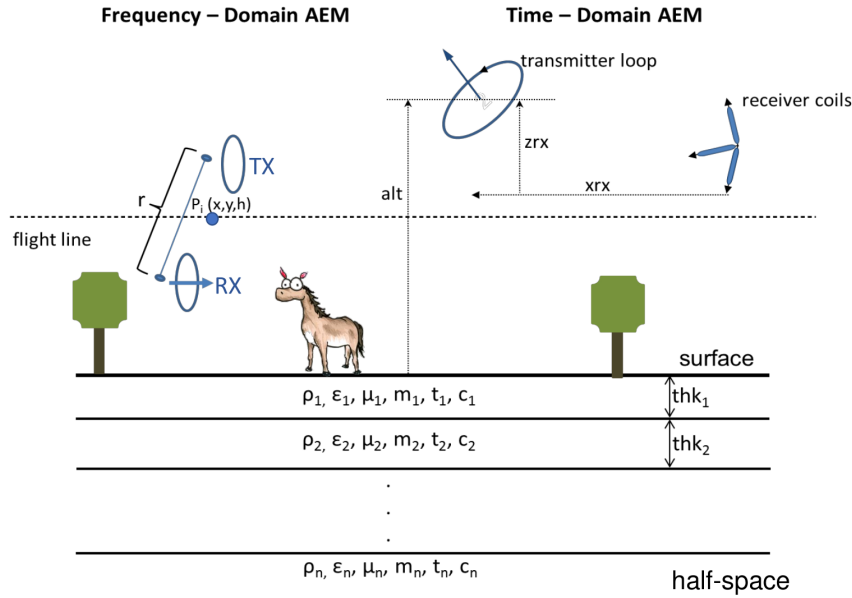


Figure 10: Schematic view of a VCP loop configuration over a layered-earth model. The AEM response is positioned at the centre between the Transmitter (TX) and Receiver (RX). The spacing ( $r$ ) between them is constant. For the Tellus FDEM Surveys,  $r \approx 21.4$  m. The survey design parameters for the FDEM data acquisition in Ireland are a nominal flight altitude of 60 m above the ground level and flight lines with a fixed orientation of 345° (NNW-SSE), perpendicular to the most common lithological and structural trends in Ireland), and a 200 m lateral spacing. The FDEM system, AEM-05 system, operates at four frequencies, (912 Hz, 3005 Hz, 11,962 Hz, and 24,510 Hz). The TDEM systems, CGG GENESIS operates at eleven Tellus time windows (0.009, 0.026, 0.052, 0.095, 0.156, 0.243, 0.365, 0.547, 0.833, 1.259, 1.858). A nominal flight altitude of 90 m above ground level was used for the TDEM data acquisition at eleven Tellus time windows for each component,  $B_{\text{inline}}$  and  $B_{\text{vertical}}$ .

On the data input side of the inversion, any of the individual eight FDEM data and eleven TDEM data can be flagged as active or inactive for the inversion (all eight components were flagged active for the FDEM inversions and only vertical TDEM data were flagged active for TDEM inversions) and data errors for the eight FDEM components and eleven TDEM components can be individually specified. EM measurement sites can be excluded from the inversion using flight clearance and powerline monitor thresholds. The theoretical and numerical basis for the Tikhonov-type inversion scheme implemented in aempy is outlined in detail (Kiyan and Rath, 2017)<sup>22</sup>, (Kiyan et al., 2022)<sup>3</sup>. There are three parameters requiring definition that control the inversion and the characteristics of the output models: the data errors, and the two regularisation parameters,  $\tau_0$  and  $\tau_1$ .  $\tau_0$  parameter controls the closeness of the inversion model to the a priori (starting) model (i.e., it controls the freedom to diverge from the starting model). Larger  $\tau_1$  values allow less freedom to diverge from the starting model.  $\tau_1$  parameter controls the 1-D model smoothness. Larger  $\tau_1$  values produce smoother models. The values that might be assigned to the regularisation parameters depend on the particular characteristics of the EM dataset being modelled (e.g., frequencies/time channels used and data errors) and on the parameterisation of the model space (e.g., number of layers, layer thicknesses, and starting model). Assignment of a data error to each of the EM data components controls the weighting placed on those components in the inversion. For example, lower errors assigned to higher frequency or early time channels data will tend to weight the inversion towards resolving shallower resistivity structure, and lower errors assigned to lower frequency data or late time channels will tend to weight the inversion towards resolving deeper structures.

## 5 RAFTA Project

As briefly described in Section 3, over the past decade, Geological Survey Ireland (GSI) has acquired and continues to acquire frequency- and time-domain airborne electromagnetic (AEM) data as part of the geophysical surveys of the Tellus programme. The overarching objective of the RAFTA (Resolution Analyses for Frequency- and Time-domain Airborne Electromagnetic Data of the Irish Tellus Programme) project is to examine the resolution capabilities of both the frequency- and time-domain AEM data of the Tellus programme. The project considers all aspects of the data, including flight height, system noise, and anthropogenic noise, which affect the resolution.

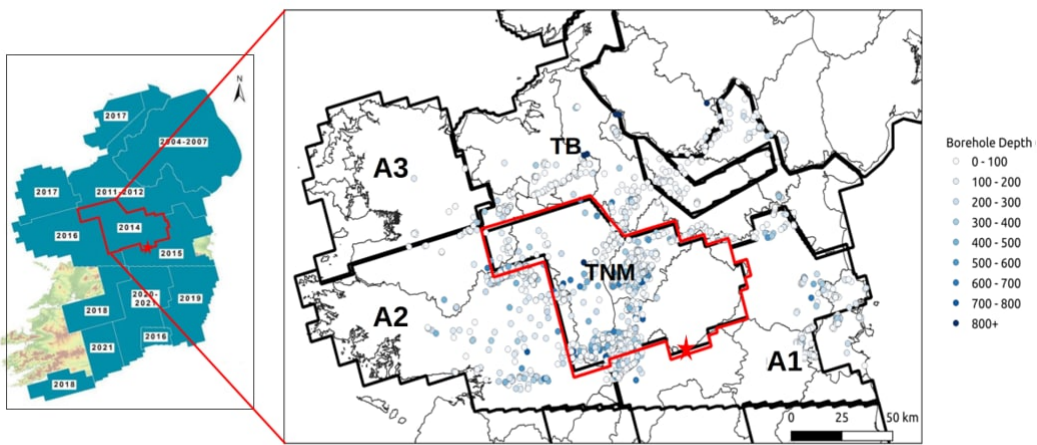


Figure 11: Tellus survey blocks and boreholes in the study area (from the GSI “verified” borehole database). TDEM data are available within the TNM survey block, and FDEM data are available within the TB (Tellus Border), A1, and A2 survey blocks. Red stars on the maps show the study area.

With the aim of collecting comparative ground data for the Tellus AEM surveys, a ground Electrical Resistivity Tomography (ERT) survey was undertaken in September 2022 along the 470 m portion of the Tellus survey lines. The time-domain AEM data were collected as part of the North Midlands survey of the Tellus programme in 2014 and the frequency-domain AEM data were collected as part of the Block A1 of the Tellus programme in 2015. In the following subsections, inversion results from both AEM systems and the influence of flight altitude parameters and data error assumptions on the resulting inverted subsurface models are discussed using synthetic and observed Tellus AEM data sets. Also, the resistivity structure of the subsurface along the Tellus AEM survey lines are compared with the resistivity structure imaged by the ERT data.

### 5.1 Synthetic AEM Data

This section discusses the forward modeling responses of both FDEM and TDEM synthetic data simulated based on two different three-layer earth models. Idealised 1-D earth models, used in this study, assume that all isotropic horizontal layers are electrically homogeneous. The simulation results of the models are inverted and, then the effect of flight altitude and inversion parameters (i.e., data error assumption) on the inversion results are discussed. Forward modelling simulation to create synthetic data starts with choosing input model parameters including, the number of layers, layers thickness, and

resistivity of layers. Altitude is chosen as the varying parameter. Then created synthetic data are inverted using the Tikhonov-type inversion. Finally, an electrical conductivity model is created and modelled at a single measurement location. The Tellus FDEM and TDEM data provided by GSI are inverted using the same deterministic approach to achieve an electrical conductivity model. The workflow followed in this study is summarised in Figure 12.

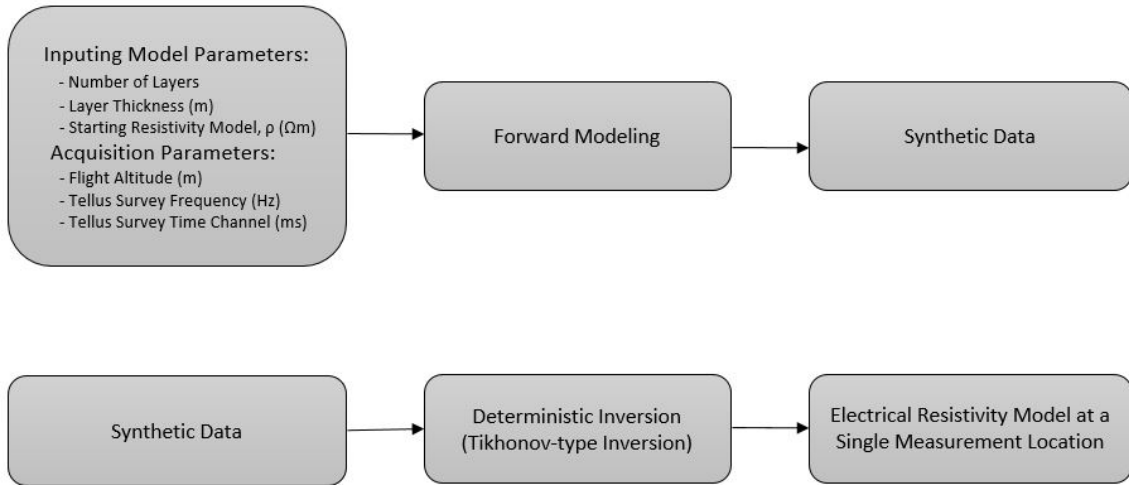


Figure 12: The workflow followed in this study. Forward modelling simulation to create synthetic data starts with choosing input model parameters including, the number of layers, layer thickness, and resistivity of layers. Altitude is chosen as the varying parameter. Then created synthetic data is inverted using the Tikhonov-type inversion. Finally, an electrical conductivity model is created and modelled at a single measurement location. The Tellus FDEM and TDEM data provided by the GSI are also inverted using Tikhonov-type inversion to achieve an electrical conductivity model of the subsurface.

Figure 13 summarise the computed forward responses for FDEM and TDEM data for two different three-layer models in Figures 13A and 13B. The resistivity model in Figure 13A comprises a 15 m thick first layer with a resistivity of 100  $\Omega\text{m}$ , a 25 m thick middle layer with a resistivity of 5  $\Omega\text{m}$ , and a lower half-space with a resistivity of 100  $\Omega\text{m}$ . The resistivity model in Figure 13B with the aim of examining the resolution of deeper layers, comprises a 50 m thick first and second layers with a resistivity of 100  $\Omega\text{m}$ , and 10  $\Omega\text{m}$  respectively, and a lower half-space with a resistivity of 1000  $\Omega\text{m}$ . Figure 13C shows the computed forward responses of the models for in-phase and quadrature components of FDEM data at four frequencies and Figure 13D shows the in-line and vertical components of TDEM data at the eleven Tellus time channels. For both datasets, the model A response is higher than model B, which could be due to the differences in the conductivity of the middle layer and the depth of the conductive layer. Generally, the existence of a conductive layer between two resistive layers increases the amplitude of data and by increasing the depth of the conductive layer, lower responses will be detected in the receiver.

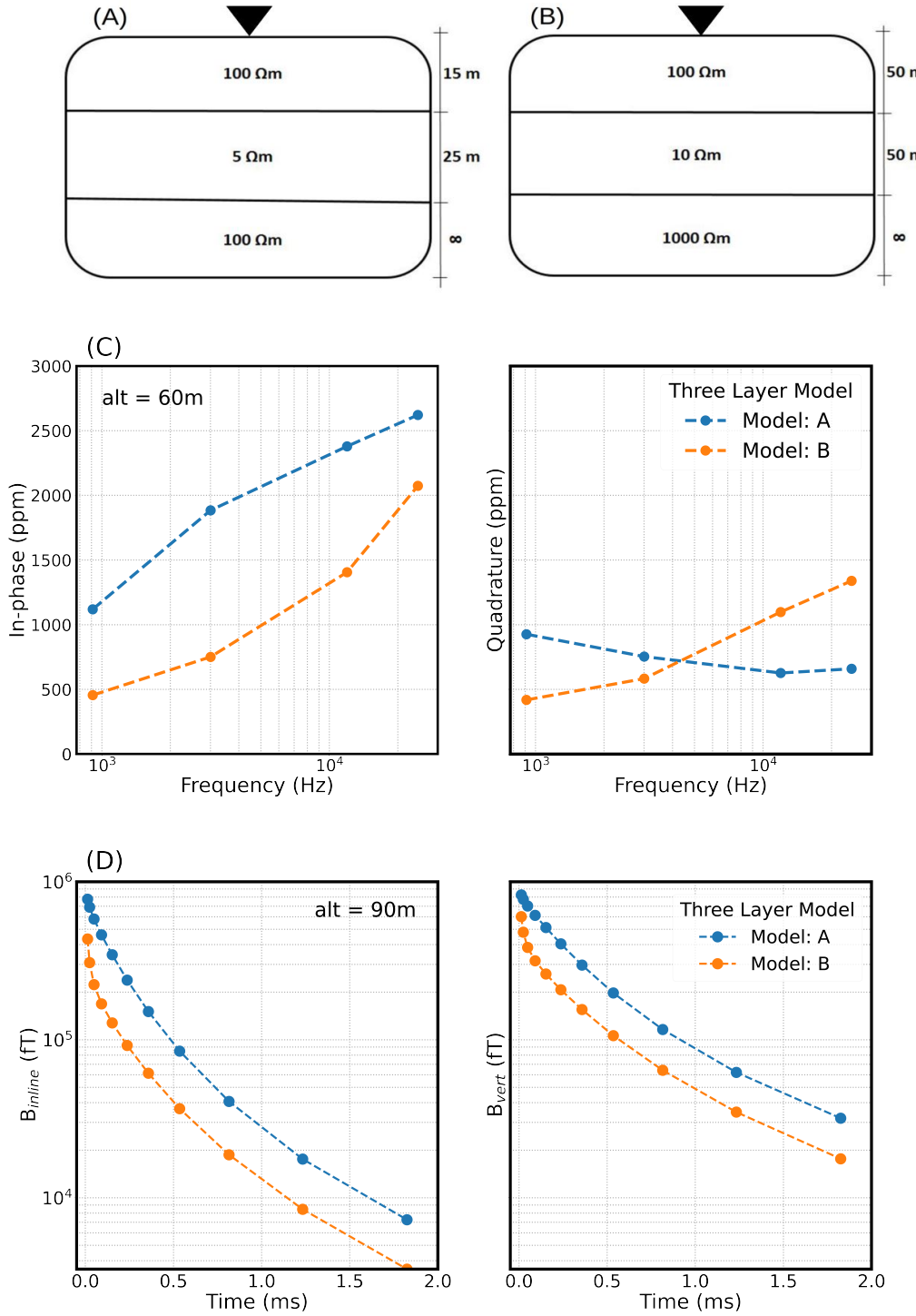


Figure 13: (A) A simple three-layer model with a lower half-space layer with a resistivity of  $100 \Omega\text{m}$ . The first layer is 15 m thick, with a resistivity of  $100 \Omega\text{m}$ . The middle layer is 25 m thick, with a resistivity of  $5 \Omega\text{m}$ . (B) A simple three-layer model with a lower half-space layer with a resistivity of  $1000 \Omega\text{m}$ . The first and second layers are 50 m thick, with a resistivity of  $100 \Omega\text{m}$  and  $10 \Omega\text{m}$  respectively. (C) Computational FDEM forward responses of models A and B. (D) Computational TDEM forward responses of models A and B.

The effect of flight altitude on the AEM response in the Bundoran test line survey

(Kiyan et al., 2022)<sup>3</sup> proved that the flight altitude significantly affects the quantity and quality of the observed data and subsequently, resulting electrical conductivity models. In this study, a simple three-layer model presented in Figure 13A is used to demonstrate the effect of different flight altitudes on the FDEM and TDEM data responses. Forward modelling is carried out for 100 model samples at nine altitudes (60 m, 70 m, 80 m, 90 m, 100 m, 120 m, 150 m, 180 m, and 240 m) for FDEM data and six different altitudes (90 m, 100 m, 120 m, 150 m, 180 m, and 240 m) for TDEM data. For FDEM data, both in-phase and quadrature components of the data are randomly perturbed by the noise of 30 ppm for all frequencies. Note that 30 ppm is a simplified error assumption for this synthetic data. For TDEM data, the error value was estimated by trial-and-error and for this model, the data is randomly perturbed by the noise of 15000 fT.

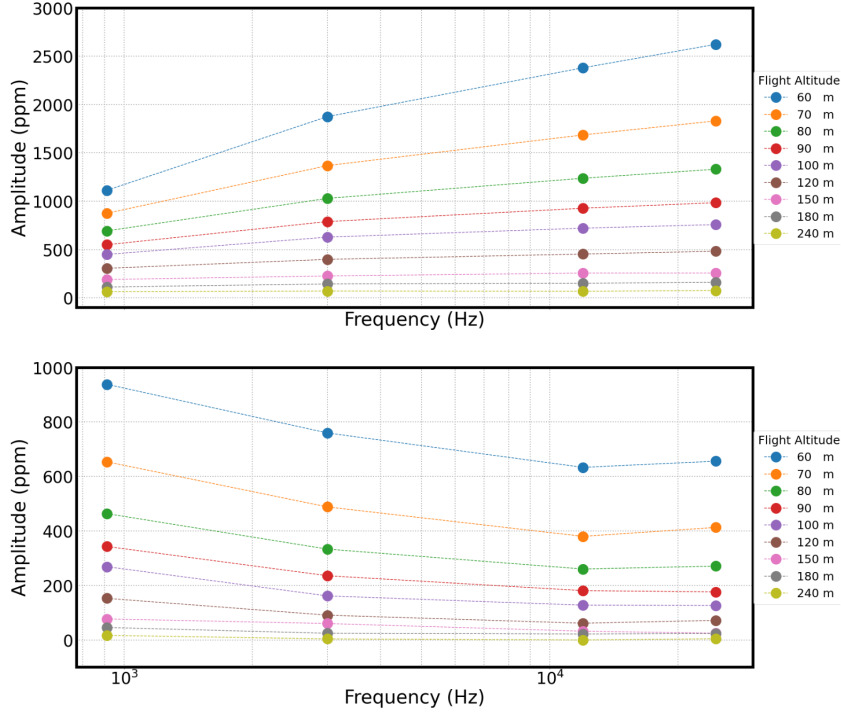


Figure 14: The forward responses of the model (Fig 13A) were calculated at four Tellus survey frequencies (912 Hz, 3005 Hz, 11962 Hz, and 24510 Hz) for nine different flight altitudes.

Comparing Figures 14 and 15 clearly shows the effect of flight altitude on the AEM response of both datasets. The figures indicate that for the lower altitude, 60 m for FDEM and 90 m for TDEM, a stronger signal at the receiver can be observed than at the highest altitude of 240 m. In addition, comparing in-phase and quadrature components of FDEM data shows that in-phase components are affected more than the quadrature components as the in-phase data amplitude ranges over approximately 2500 ppm, while the quadrature component approximately 900 ppm.

Figure 16 summarises the Tikhonov-type inversion results of synthetic FDEM data for the simple three-layer resistivity model illustrated in Figure 13A. The simulated airborne system is the one used for the Tellus surveys: two pairs of co-planar coils operating at four frequencies with TX – RX separation of  $\approx 21.4$  m. In-phase and quadrature components were randomly perturbed by the noise of 30 ppm. The data were inverted using 1-D smooth, multi-layer Tikhonov-type inversion. The model consists of 50 layers with the thickness of the top layer starting at 5 m and subsequent layers increasing logarithmically

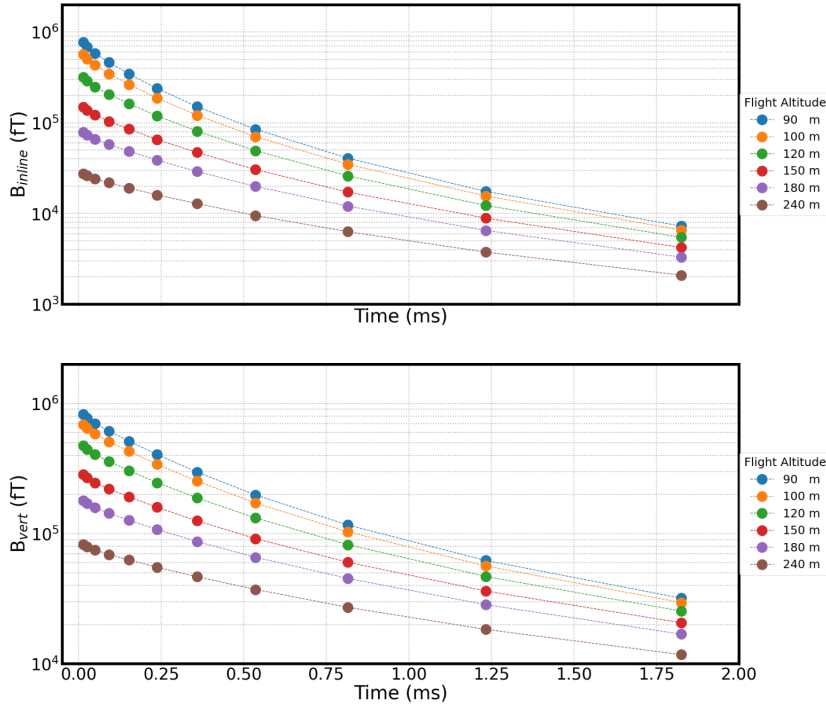


Figure 15: Computed in-line and vertical components of TDEM data of the model given in Figure 13A for six different flight altitudes. The data were calculated at eleven Tellus survey time channels.

in thickness with a depth till 360 m. The layer thicknesses were preserved during the inversion process. A prior resistivity of 100 m was chosen. The inversion results for the altitudes of 60 m, 90 m, and 150 m for 100 model samples are presented on the left panel of Figure 16. The inversion result obtained with 60 m and 90 m flight altitudes show the presence of three layers with different resistivity values. Inverted models indicate that the resistivity values of the first and second layers are estimated with a relatively acceptable approximation for these low-flight altitudes. The resistivity of the middle layer has been estimated more accurately, and the inverted data show the presence of a conductive middle layer. The resistivity of the bottom layer has not been precisely determined due to the presence of a highly conductive (or its inverse less resistive, 5  $\Omega\text{m}$ ) middle layer which has a strong impact on the resolution of the bottom layer. For the higher altitude, 150 m, there is a noticeable deviation from the true model for each of the three layers. As mentioned, for FDEM data in higher altitudes weaker signals can be detected so FDEM data acquired at the flight altitude of 150 m appear to be too weak to recover the subsurface resistivity values.

Inversion results at flight altitudes of 70 m, 80 m, 100 m, 120 m, 180 m, and 240 m can be found in Appendix C. The range of flight altitudes used for the simulation was selected as it corresponds with the range of altitudes theoretically flown during the Tellus survey.

The summary of all altitudes is illustrated on the left panel of Figure 17. Comparing the median value for each altitude with the true model shows a clear contrast between the recovered subsurface conductivity models for higher altitudes. It is therefore recommended, if possible, to carry out AEM investigation at altitudes lower than 100 m. In this study, the forward responses of the three-layer model with 60 m flight altitude were perturbed using several error values chosen after the statistical analysis using the 240 m clearance data flown in 2015 across the onshore region of the Tellus Bundoran test line (Kiyani et al., 2022)<sup>3</sup>. The inversion results are illustrated on the right panel of Figure 17.

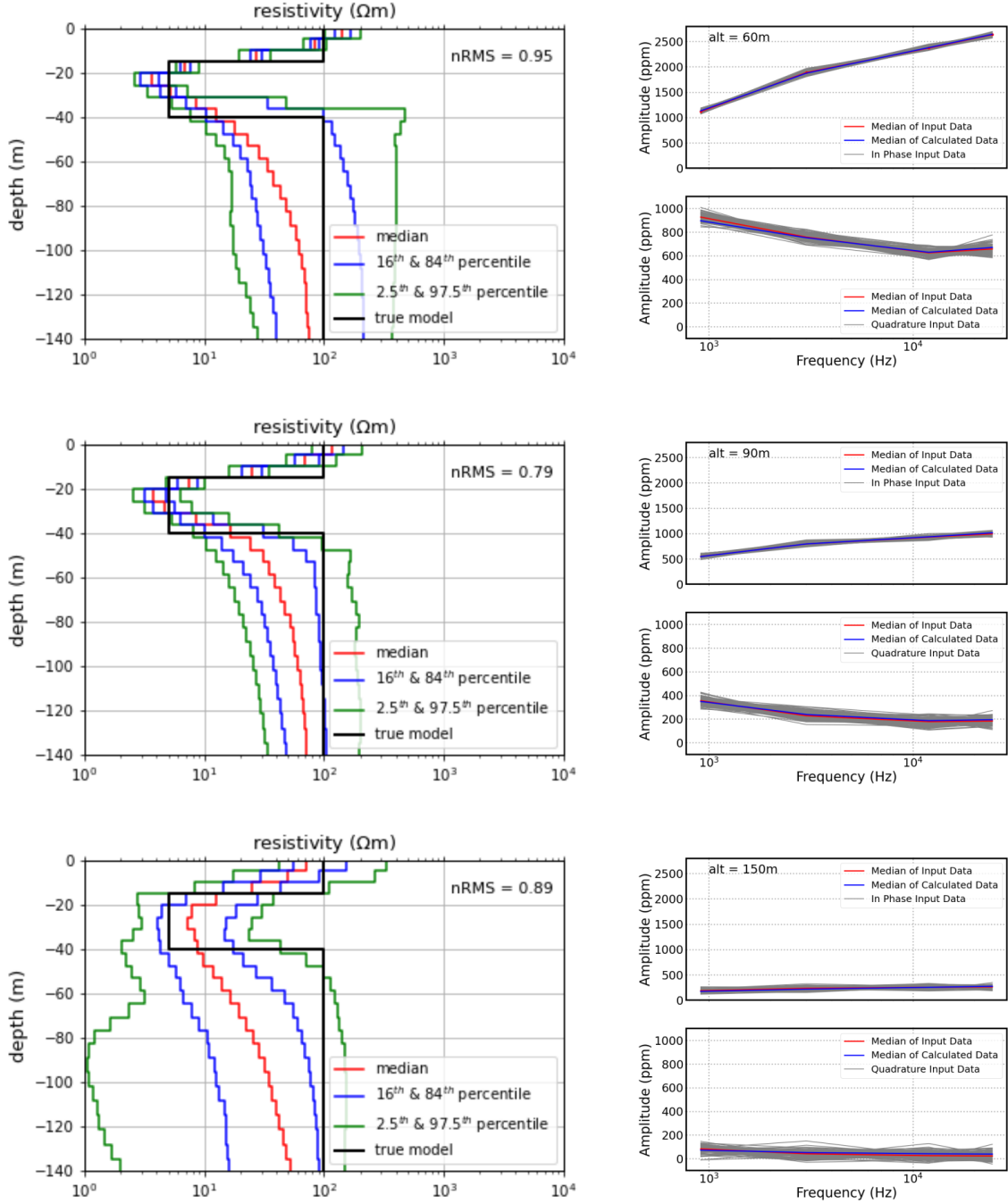


Figure 16: Tikhonov-type inversion results for a three-layer model at the altitudes of 60 m, 90 m, and 150 m for 100 model samples of FDEM synthetic data. The plots on the left-hand side show the true model with the solid black line and the median resistivity values of 100 model samples with the solid red line. The bounds that contain 68 and 98 percent of the 100 model samples are shown with a blue and green solid line, respectively. The right panel illustrates the data fit. The input data responses of 100 model samples are represented with grey solid lines and the median of the data is represented with a red solid line. The median of predicted data is represented with the blue solid line. The data error assumption was 30 ppm and regularisation parameters,  $\tau_0 = 0.01$ , and a range of  $\tau_1 = 0.1\text{-}100$  were chosen.

The recovered subsurface resistivity model with 20 ppm error assumption is similar to the resistivity model with 70 ppm error assumption.

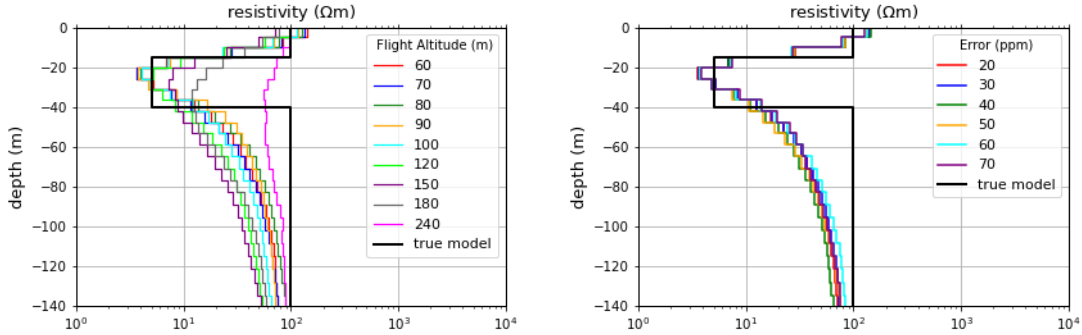


Figure 17: Summary of the output from the Tikhonov-type inversion, which was run for 100 model samples. Left panel: The inversion results of all altitudes showing the median value of the 100 model samples. The data error assumption was 30 ppm. Right panel: The inversion results of different data error assumptions showing the median value of the three-layer model for the flight altitude of 60 m. The regularisation parameters,  $\tau_0 = 0.01$ , and a range of  $\tau_1 = 0.1\text{-}100$  were chosen.

Forward simulation and Tikhonov-type inversion results of TDEM synthetic data based on the resistivity model in Figure 13A are in Figure 18. The in-line and vertical components of the synthetic TDEM data were computed at eleven Tellus survey time channels and were then randomly perturbed by the noise of 15000 fT. The data were inverted using 1-D smooth, multi-layer Tikhonov-type inversion. The model consists of 50 layers with the thickness of the top layer starting at 5 m and subsequent layers increasing logarithmically in thickness with a depth till 360 m. The layer thicknesses were preserved during the inversion process. A prior resistivity of 100 m was chosen. The flight altitudes used for the simulations are 90 m, 150 m, and 180 m.

The inversion results show that the conductive middle layer in Figure 13A has successfully recovered. As expected, the inversion of 90 m flight altitude data does a much better job of recovering the conductive middle layer. Inverted models clearly detect the layers of the resistivity model. The 90 m flight altitude result seems to recover the model more accurately when referring to the resistivity and the thickness of the first two layers. Although due to the highly conductive middle layer the resistivity of the bottom layer has not been correctly recovered, the recovered resistivity values are more accurate than FDEM data at greater depths. Although there are deviations from the true model for the higher altitudes (i.e., 150 m and 180 m), the TDEM data inversions still recover the true model better than FDEM data inversion at the flight altitude of 150 m. The results of inverted data at flight altitudes of 100 m, 120 m, and 240 m can be found in Appendix D.

The summary of all the altitudes is illustrated on the left panel of Figure 19. Comparing the median value for each altitude with the true model shows a clear contrast between the recovered subsurface conductivity models for higher altitudes. Similar to FDEM data, acquired TDEM data at altitudes lower than 100 m do a better job when recovering the model. One can also clearly see that the FDEM data inversions perform better than the TDEM data inversions for recovering the resistivity value of the top layer. In this study, the forward responses of the three-layer model with 90 m flight altitude were perturbed using several error values chosen after trial-and-error. The inversion results for different data error assumptions are illustrated on the right panel of Figure 19.

Considering that TDEM data generally provide much deeper resolution compared to FDEM data, and is more sensitive to greater depth, TDEM data have also been simulated and inverted based on the simple three-layer resistivity model in Figure 13B. In-line and vertical components of the synthetic TDEM data were computed at eleven Tellus survey

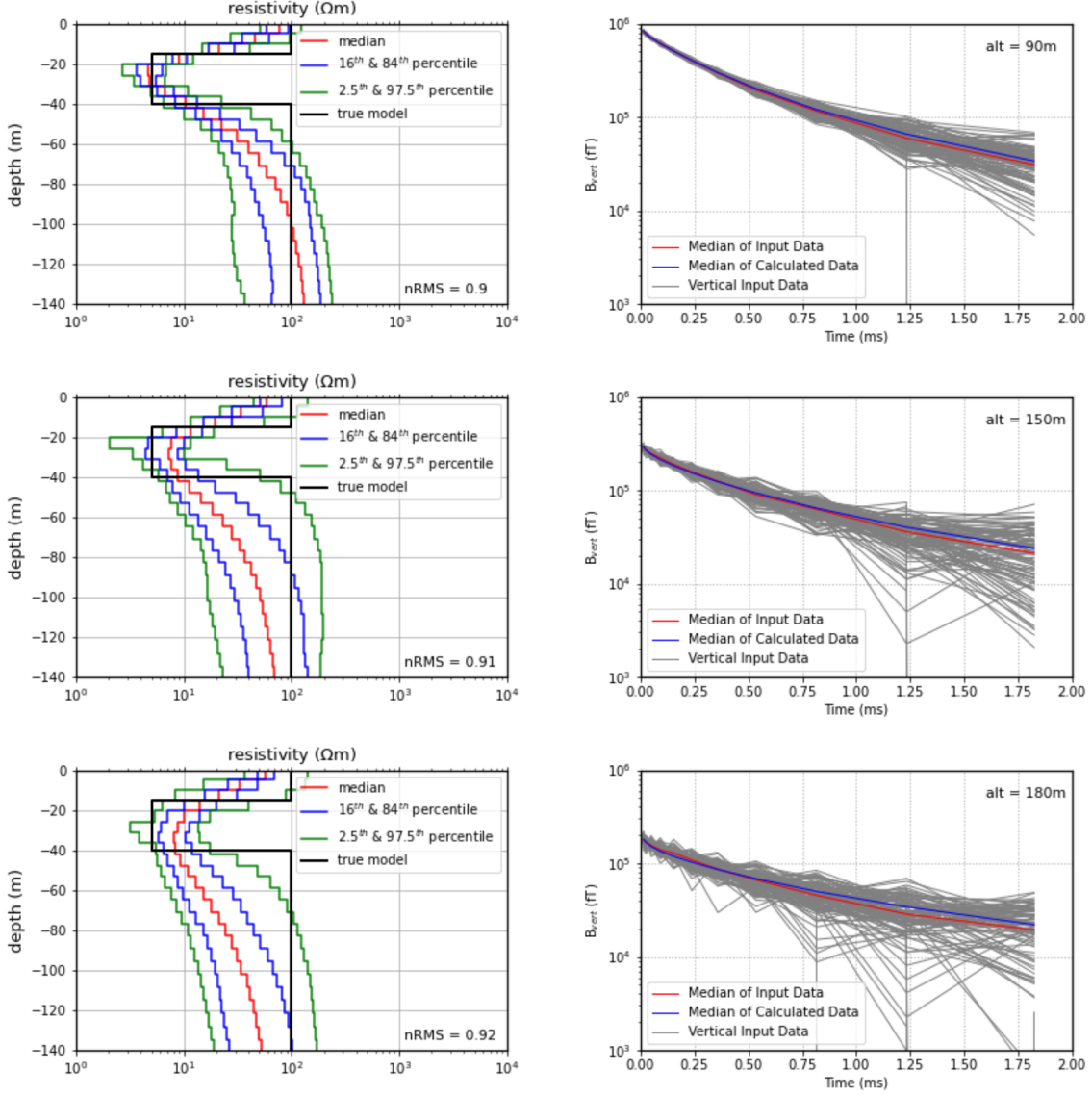


Figure 18: Tikhonov-type inversion results for a three-layer model at the altitudes of 90 m, 150 m, and 180 m for 100 model samples of TDEM synthetic data. The plots on the left-hand side show the true model with the solid black line and the median resistivity values of 100 model samples with the solid red line. The bounds that contain 68 and 98 percent of the 100 model samples are shown with a blue and green solid line respectively. The right panel illustrates the data fit and median of the data. 100 model samples are represented with grey solid lines and the median of the data is represented with a red solid line. The median of predicted data is represented with the blue solid line. The data error assumption was 15000 fT and regularisation parameters,  $\tau_0 = 0.01$ , and a range of  $\tau_1 = 0.1\text{-}100$  were chosen.

time channels and were then randomly perturbed by the noise of 3000 fT. The data were inverted using 1-D smooth, multi-layer Tikhonov-type inversion. The model consists of 50 layers with the thickness of the top layer starting at 5 m and subsequent layers increasing logarithmically in thickness with a depth till 360 m. The layer thicknesses were preserved during the inversion process. A prior resistivity of 100 m was chosen. The flight altitudes used for the simulations are 90 m, 150 m, and 180 m.

The inversion results in Figure 20 show that the resistivity values and the thickness of

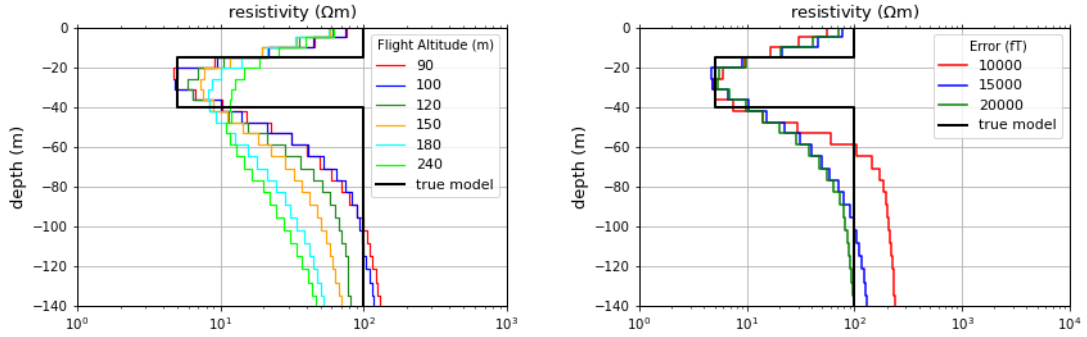


Figure 19: Summary of the output from the Tikhonov-type inversion, which was run for 100 model samples. Left panel: The inversion results of all altitudes showing the median value of the 100 model samples. The data error assumption was 15000 fT. Right panel: The inversion results of different data error assumptions showing the median values of the 100 model samples for the flight altitude of 90 m. The regularisation parameters,  $\tau_0 = 0.01$ , and a range of  $\tau_1 = 0.1\text{--}100$  were chosen.

layers have been estimated with a high approximation for the first and second layers. As we mentioned in this model (Fig. 13B) the depth of the first and second layers together reaches 100 m, and inversion results recover the true model with a relatively high approximation till this depth at 90 m flight altitude. For 150 m, although the second layer values are underestimated, the first layer especially at the depth of 25 m has been estimated successfully. The resistivity of the bottom layer has not been accurately resolved; that could be due to the highly conductive middle layer or 100 m thickness of the two first layers, which decreases the resolution of the bottom layer.

The summary of all altitudes is illustrated on the left panel of Figure 21. Comparing the median value for each altitude with the true model shows a contrast between the recovered subsurface conductivity models for altitudes higher than 150 m at a depth of more than 50 m. In this study, the forward responses of the three-layer model with 90 m flight altitude were perturbed using several error values chosen after trial-and-error. The inversion results for different data error assumptions are illustrated on the right panel of Figure 21.

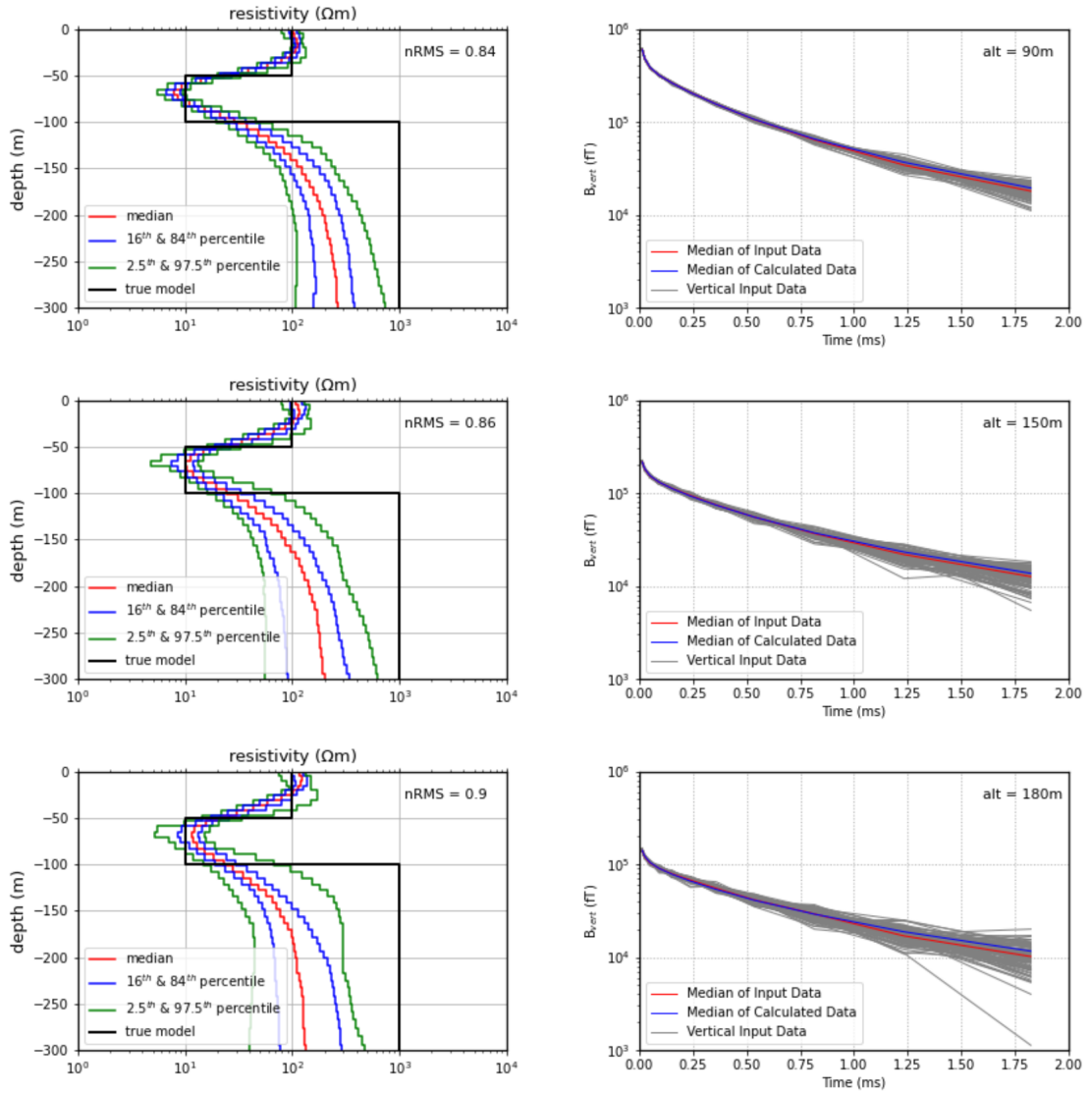


Figure 20: Tikhonov-type inversion results for a three-layer model at the altitudes of 90 m, 150 m, and 180 m for 100 model samples of TDEM synthetic data. The plots on the left-hand side show the true model with the solid black line and the median resistivity values of 100 model samples with the solid red line. The bounds that contain 68 and 98 percent of the 100 model samples are shown with a blue and green solid line, respectively. The right panel illustrates the data fit and median of the data. 100 model samples are represented with grey solid lines and the median of the data is represented with a red solid line. The median of predicted data is represented with the blue solid line. The data error assumption was 3000 fT and the regularisation parameters,  $\tau_0 = 0.01$ , and a range of  $\tau_1 = 0.1\text{--}100$  were chosen.

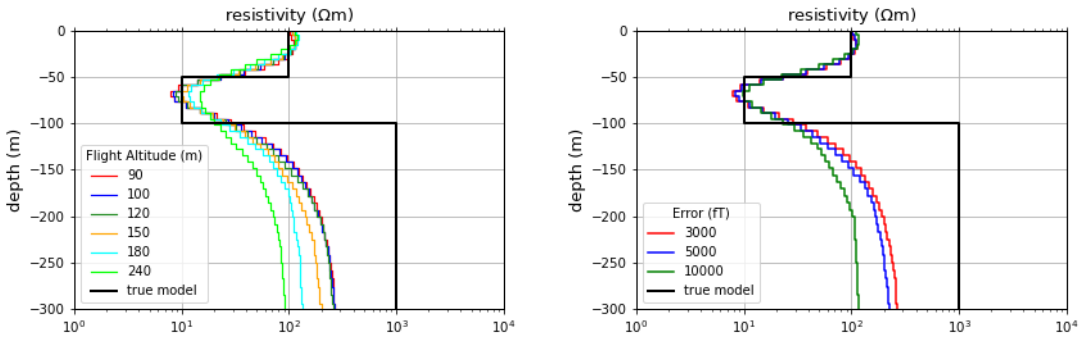


Figure 21: Summary of the output from the Tikhonov-type inversion, which was run for 100 model samples. Left panel: The inversion results of all altitudes showing the median values of the 100 model samples. The data error assumption was 3000 fT. Right panel: The inversion results of different data error assumptions showing the median values of the 100 model samples for the flight altitude of 90 m. The regularisation parameters,  $\tau_0 = 0.01$ , and a range of  $\tau_1 = 0.1\text{-}100$  were chosen.

## 5.2 Observed AEM Data and Electrical Resistivity Tomography (ERT) Data

### 5.2.1 Survey Area

The Tellus AEM survey lines investigated in this study are located approximately 20 km southeast of Athlone, close to Clara, Co. Offaly. The AEM lines are 1470 m long and the three ERT profiles were acquired along the 470 m portion of the Tellus AEM survey lines (Figs. 22 and 23). According to GSI 1:100,000 Bedrock Geology map (Fig. 22) the Tellus AEM survey lines traverse one distinct lithological unit. The AEM survey lines are underlain by thick-bedded limestone of the Allenwood Formation. The northernmost 120 m (approximately) of the lines is underlain by massive unbedded lime-mudstone of Waulsortian Fomation. The subsoil geology in the area (Fig. 23) is dominated by alluvium deposits (approximately 620 m portion of the lines from their northern ends and 120 m portion of the lines from their southern end) and till derived from limestones (660 m portion of the AEM lines).

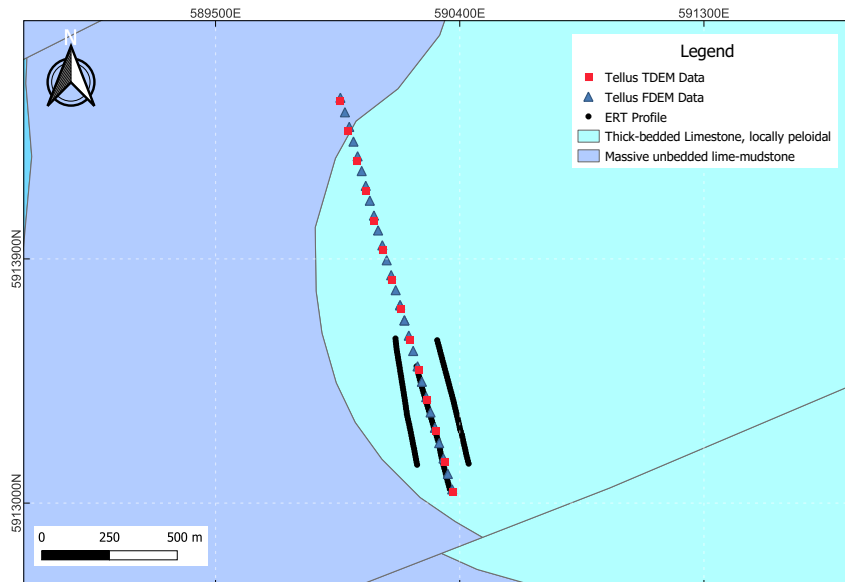


Figure 22: Bedrock Geology (GSI, 1:100,000) map of the study area with the locations of frequency- and time-domain AEM data measurement points and the ERT profiles. The center profile is almost identical to the overlap flight line, where both FDEM and TDEM data are available. In order to get a quasi-3-D picture of the subsurface, two parallel ERT profiles were measured at a distance of approximately 10 m. The map was created with QGIS.

### 5.2.2 Tellus FDEM and TDEM Data Inversion

Tellus FDEM and TDEM airborne data sets were inverted from flight lines No: L1126 and No: L13490, respectively (Figs. 22 and 23). 1-D models of resistivity variation with depth were derived independently and were subsequently gridded together to produce pseudo 2-D resistivity sections. Figure 24 shows the electrical resistivity model from the inversion of Tellus FDEM data along the 1400 m flight line. Inversions were carried out using both in-phase and quadrature components of FDEM data at four frequencies (24510 Hz, 11962 Hz, 3005 Hz, and 912 Hz). The starting model consists of 32 layers with the thickness of the top layer starting at 2 m and subsequent layers increasing logarithmically in thickness

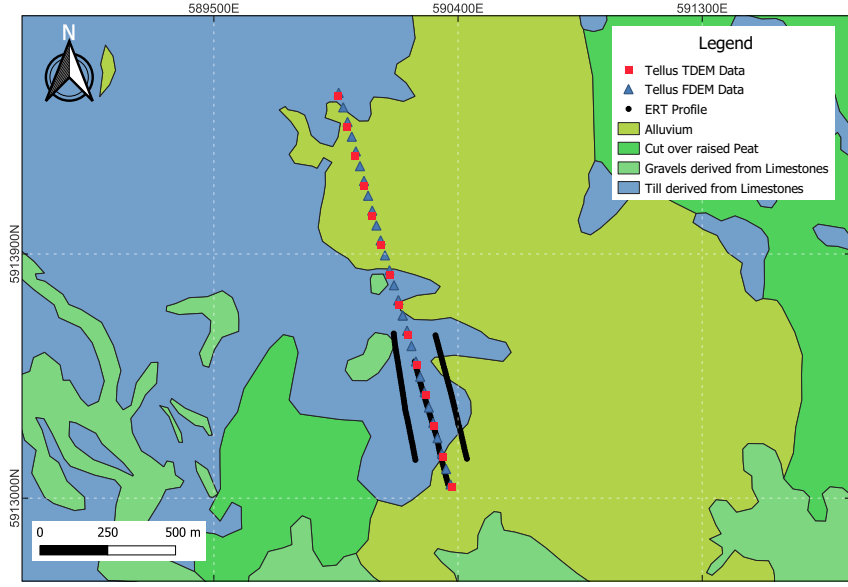


Figure 23: Quaternary Geology (GSI, 1:50,000) map of the study area with the locations of frequency- and time-domain AEM data measurement points and the ERT profiles. The center profile is almost identical to the overlap flight line, where both FDEM and TDEM data are available. In order to get a quasi-3-D picture of the subsurface, two parallel ERT profiles were measured at a distance of approximately 10 m. The map was created with QGIS.

with depth till 160 m. The layer thicknesses have been preserved during the inversion process. A prior resistivity of 100 m was chosen and each site was modeled independently. The data error assumption was 50 ppm. Regularisation parameters,  $\tau_0 = 0.01$  and  $\tau_1 = 0.1\text{-}100$  were chosen by trial-and-error. Note that the inverted models derived from the FDEM data were reconstructed using the first two singular values and vectors (Kiyan et al., 2022)<sup>3</sup>.

Figure 25 shows the electrical resistivity model from the inversion of Tellus TDEM data along the 1400 m flight line. Only vertical components of the Tellus TDEM data were inverted. The starting model consists of 30 layers with the thickness of the top layer starting at 4 m and subsequent layers increasing logarithmically in thickness with depth till 160 m. The layer thicknesses have been preserved during the inversion process. A prior resistivity of 300 m was chosen and each site was modeled independently. The data error assumption was 100 fT. Regularisation parameters,  $\tau_0 = 0.01$  and  $\tau_1 = 0.1\text{-}100$  were chosen by trial-and-error.

Note that TDEM data inversions were carried out with the vertical (Z) component data only, as the in-line (X) component data are smaller than the vertical data and the negative values occur mainly in the X component.

### 5.2.3 Electrical Resistivity Tomography (ERT) Data Inversion

The Electrical Resistivity Tomography method (ERT) measures the electrical resistivity (or electrical conductivity) of the subsurface using the principle of Ohm's law, which can be expressed as:

$$V = I \cdot \rho \frac{l}{A} \quad (12)$$

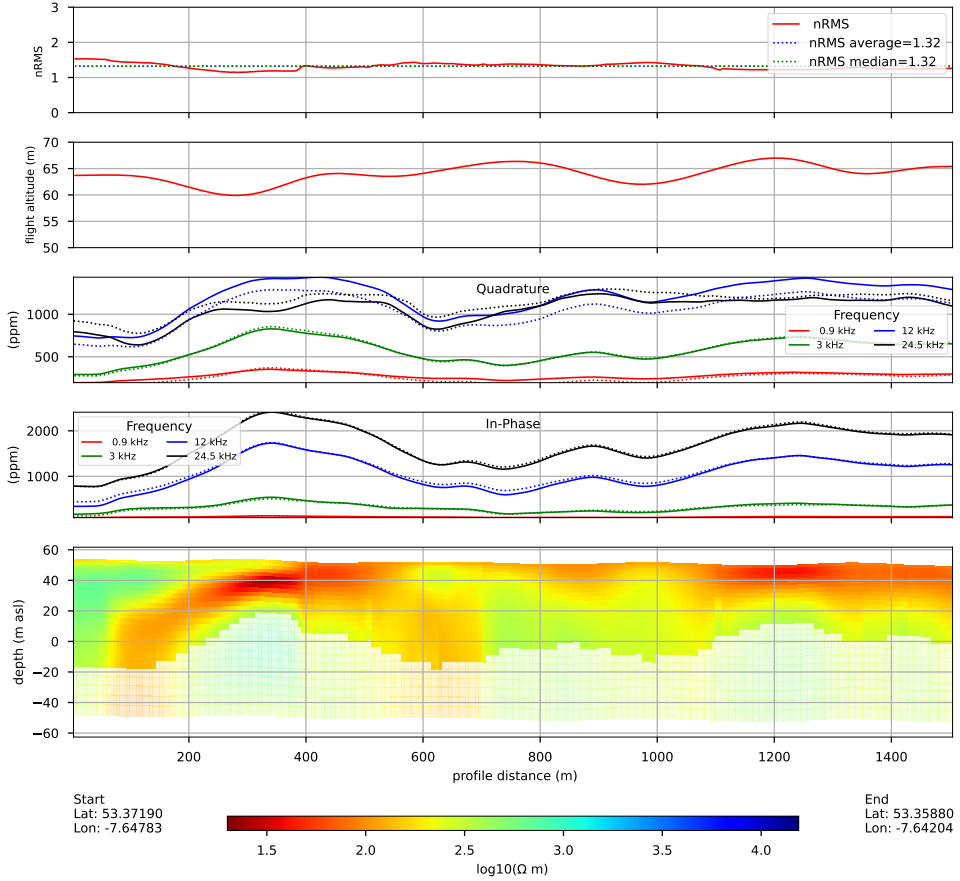


Figure 24: Electrical resistivity model from the inversion of Tellus FDEM data. Inversion regularisation parameters  $\tau_0 = 0.01$  and  $\tau_1 = 0.1\text{--}100$  were chosen. Observed (solid circles) and calculated (solid lines) data at four survey frequencies 24510 Hz, 11962 Hz, 3005 Hz, and 912 Hz, shown in black, blue, green, and red colours, respectively.

where  $V$  is the voltage measured between two electrodes (C2 and C3 in Fig. 26),  $I$  is the current applied,  $l$  and  $A$  are the path length and cross-sectional area along/through which the current flows, respectively, and  $\rho$  is the resistivity of the material through which the current passes. In this study, three ERT resistivity profiles, approximately 470 m in length, were acquired using a 48-electrode Syscal Pro system along the southern portion of the FDEM and TDEM survey lines (Figs. 22 and 23) in collaboration with the researchers from the National University Ireland, Galway. A Wenner – Schlumberger survey geometry (Fig. 26) with 10 m electrode spacing was used. In this configuration current electrodes are positioned outside of potential electrodes and the separation between the first current electrode and first potential electrode ( $na$ ) is greater than or equal to five times the potential electrode separation ( $a$ ) (Reynolds, 2011)<sup>28</sup>. This array can be used effectively for a number of applications, particularly for imaging horizontal or near horizontal layers. A dipole-dipole survey configuration was also tested however measurements could not be successfully carried out due to the instrument’s internal battery issue. The ERT survey

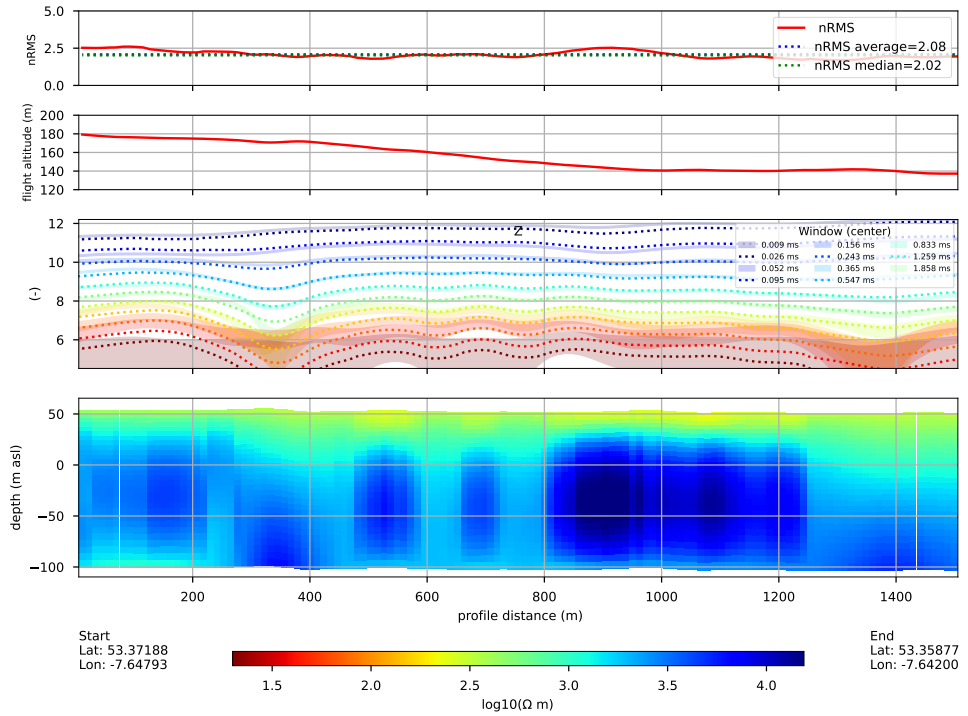


Figure 25: Electrical resistivity model from the inversion of Tellus TDEM data. Inversion regularisation parameters  $\tau_0 = 0.01$  and  $\tau_1 = 0.1-100$  were chosen. Only vertical components of TDEM data were inverted at eleven Tellus time channels. Observed (solid circles) and calculated (solid lines) data at eleven Tellus time channels shown in different colours.

details and the characteristics of the Syscal Pro system are given in Table 2 and Table 3, respectively.

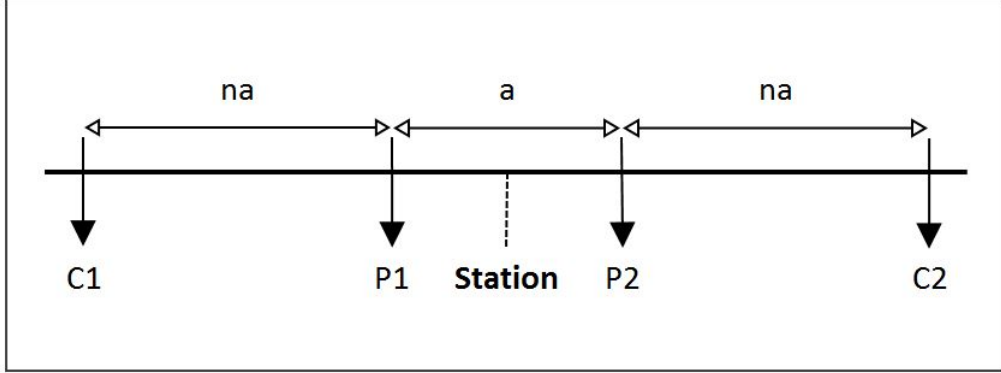


Figure 26: Wenner-Schlumberger array (source: ARES II User Manual v1.5).

The ERT data were inverted using two different 2-D inversion software, namely ResIPy (Blanchy et al., 2020) and Res2DInv (© 1995-2011 Geotomo Software). ResIPy is an intuitive open-source software for inversion and modelling of electrical resistivity and induced polarisation measurements. In ResIPy, two types of 2-D finite element meshes can

Table 2: Position of measured profiles on the test line. Coordinates of the beginning and end of each profile, the total profile length (P.L), electrode array configuration, and the number of electrodes (N.O.E) used.

ERT Profile	Start(UTM)	End(UTM)	P.L	Array/N.O.E
Main Profile	590240.5752E	590363.0804E	470m	Wenner-Schlumberger/48
	5913504.1562N	5913051.65978N		
East Profile	590316.6300E	590432.5040E	470m	Wenner-Schlumberger/48
	5913600.2149N	5913145.5821N		
West Profile	590162.8490E	590242.5284E	470m	Wenner-Schlumberger/48
	5913606.7785N	5913141.5344N		

Table 3: Characteristics of Syscal Pro System used in the ERT survey.

Characteristics of Syscal Pro System	
Transmitter	
Voltage	0 - 2000 Vpp
Current	0 - 2500 mA
Power	internal 250W DC/DC converter and 1200W with external AC/DC
Battery	internal battery or external 12V
Receiver	
Pulse duration	250ms, 500ms, 1s, 2s, 4s, or 8s
Channels	250ms, 500ms, 1s, 2s, 4s, or 8s
Channels	10 true differential inputs
Input Impedance	100 M $\Omega$ ms
Input Voltage	15V, automatic gain, input protection 1000V
Resolution	1 $\mu$ V
GPS	GPS input for coordinates and synchronisation
Readings	resistivity, self-potential, induced polarisation (up to 20 windows), quality control, and optional full waveform
Noise Rejection	power line rejection, SP linear drift correction

be used: structured quadrilateral or unstructured triangular. In this study, structured quadrilateral mesh was used. The electrical resistivity models of the three ERT profiles obtained from ResIPy and Res2DInv are presented in Figures 27 and 28, respectively. The main profile was acquired along the AEM survey lines. There is a very good agreement between the resulting resistivity models produced by the two different inversion software. The bedrock geology along the 470 m portion of the AEM profiles is mapped as the Allenwood Formation (massive, unbedded lime-mudstone). The resistivity models derived from the ERT data along the main profile show a highly resistive bedrock with resistivities greater than 5000  $\Omega$ m, which agrees with the time-domain AEM derived resistivity model, which also shows a highly resistive bedrock with a resistivity greater than 3000  $\Omega$ m. Both ERT-derived resistivity models show a conductive layer with a thickness of about 10 m along the three profiles. The thickness of this conductive layer increases at the centre of the main profile presented in Figures 27 and 28. According to the GSI Quaternary Sediments map till derived from limestones is the predominant subsoil types along the profiles. The much less resistive material (approximately 300 – 500  $\Omega$ m) along the whole profile between the depths of 40 – 30 m asl could correspond to this subsoil type. The frequency-domain AEM resistivity model shows a more conductive (approximately 50 – 150  $\Omega$ m) till units to a depth of about 25 m asl overlying a transition zone in which resistivities increase with

depth. However, the resistivity model has a lower resolution than the ERT-derived and time-domain AEM-derived resistivity models.

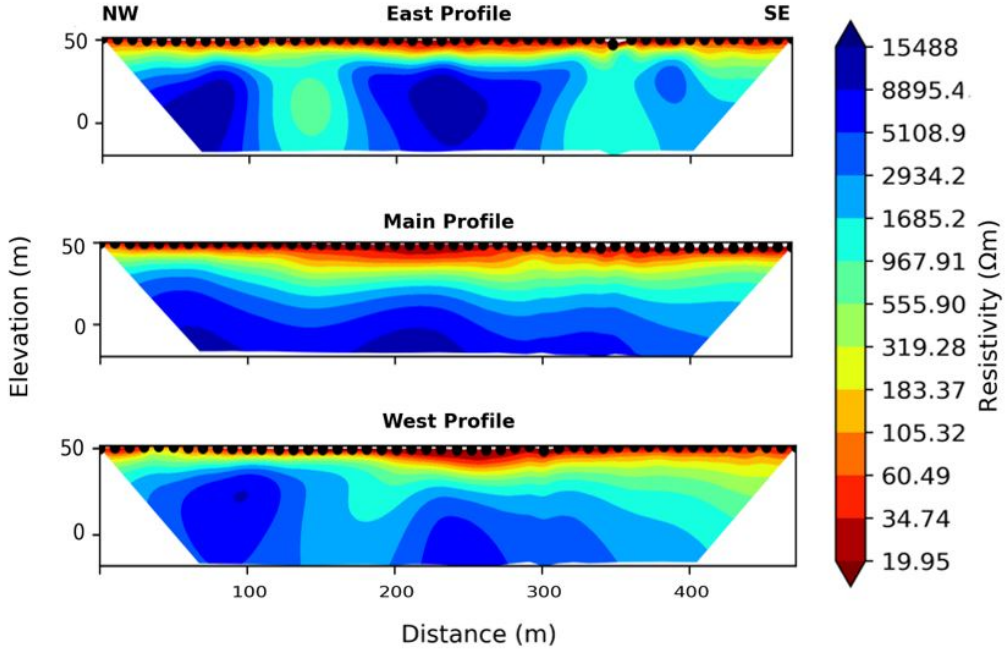


Figure 27: Electrical resistivity models from the inversion of ERT data using ResIPy software. ERT data were acquired with a 10 m spacing between electrodes using Wenner-Schlumberger configuration.

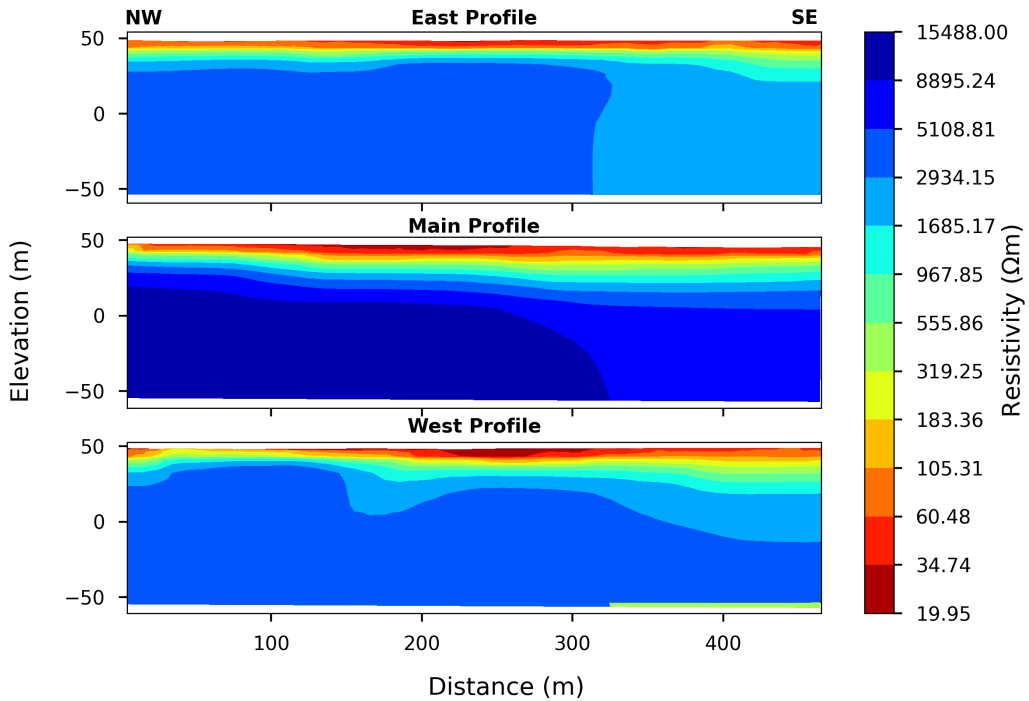


Figure 28: Electrical resistivity models from the inversion of ERT data using Res2DInv software. ERT data were acquired with a 10 m spacing between electrodes using Wenner-Schlumberger configuration.

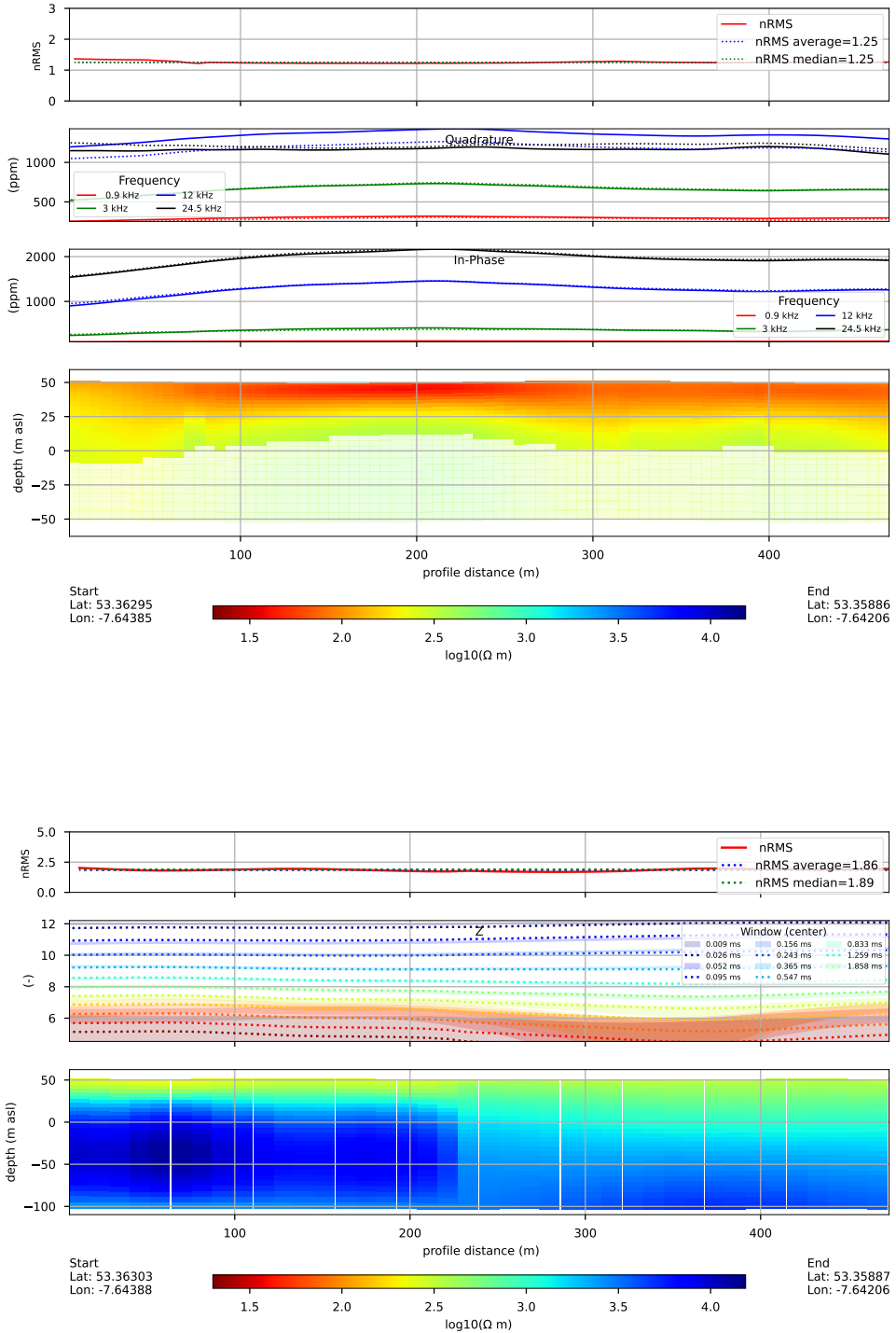


Figure 29: Electrical resistivity models from the inversion of Tellus FDEM (top) and TDEM (bottom) data consistent with the main ERT profile at the Clara survey area. Inversion regularisation parameters  $\tau_0 = 0.01$  and  $\tau_1 = 0.1\text{-}100$  were chosen.

In order to compare differences between the resistivity models obtained from AEM datasets and the ERT data acquired along the main profile, FDEM, and TDEM data were sim-

ulated using the simplified version of the ERT resistivity model beneath the electrode number 22 (Fig. 30). The number of layers, layers thicknesses, and the resistivity of the layers were calculated using the average of layers thicknesses and layer resistivities from the ERT model. Figure 30 shows the simulated simplified three-layer model, consisting of a lower half-space layer with a resistivity of  $10000 \Omega\text{m}$ . The first layer is 10 m thick with a resistivity of  $30 \Omega\text{m}$ , and the middle layer is 18 m thick with a resistivity of  $1200 \Omega\text{m}$ .

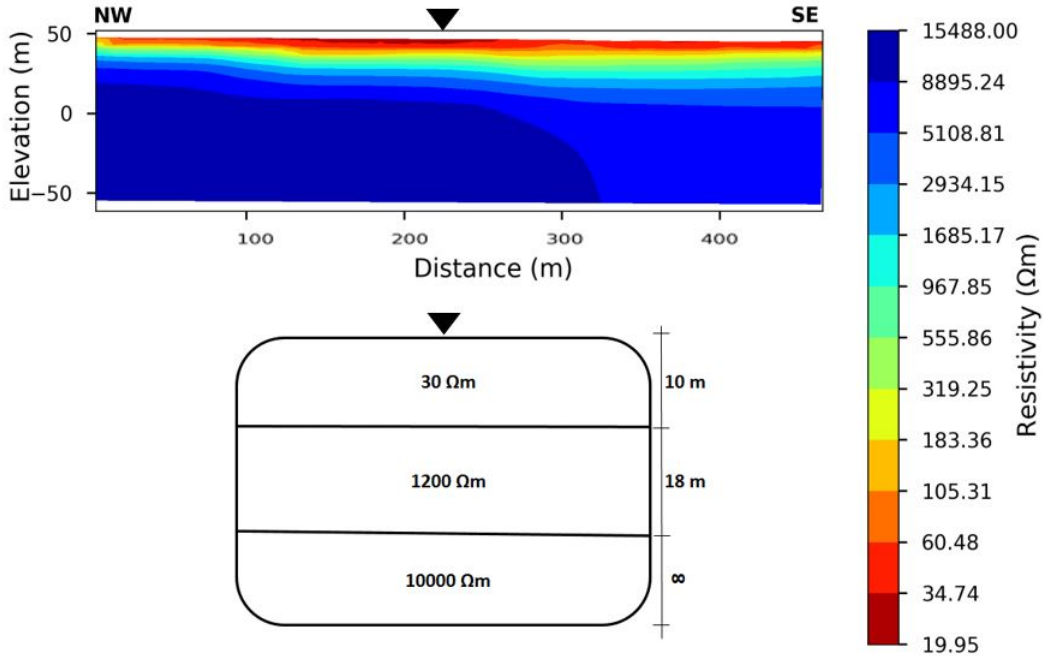


Figure 30: (Top) Electrical resistivity model from the inversion of the ERT data acquired along the main profile. (Bottom) Simulated three-layer resistivity model derived from the ERT resistivity model. The model comprises a 10 m thick first layer with a resistivity of  $30 \Omega\text{m}$ , and 180 m thick middle layer with a resistivity of  $1200 \Omega\text{m}$ , and a lower half-space with a resistivity of  $10000 \Omega\text{m}$ .

Figures 31A and B show the inversion results of the FDEM synthetic data calculated at the flight altitude of 60 m for 100 model samples. In-phase and quadrature components were randomly perturbed by the noise of 30 ppm and 50 ppm. The data were inverted using 1-D smooth, multi-layer Tikhonov-type inversion. The model consists of 50 layers with the thickness of the top layer starting at 5 m and subsequent layers increasing logarithmically in thickness with a depth till 360 m. The layer thicknesses were preserved during the inversion process. A prior resistivity of 100 m was chosen. Figure 31C compares the median response of the 100 model sample responses of simulated data based on the ERT model at one single site with the observed Tellus FDEM data collected at the same site. Although the graphs do not completely overlap, different values at different frequencies are still comparable especially for the in-phase component data except the highest frequencies (i.e., 24510 Hz and 11962 Hz). The simulated FDEM data have higher amplitudes than the observed Tellus FDEM data. As one can clearly see that FDEM data inversion can recover the shallow part of the model (especially the first 5 m), however, it struggles to find the resistivity at greater depths.

Similar to FDEM data, TDEM data were calculated at flight altitudes of 90 m and 140 m. Only vertical components of TDEM data were inverted at eleven Tellus time channels which were randomly perturbed by 100 ft. The data were inverted using 1-D smooth, multi-layer Tikhonov-type inversion. The model consists of 50 layers with the thickness of the top layer starting at 5 m and subsequent layers increasing logarithmically in thickness

with a depth till 360 m. The layer thicknesses were preserved during the inversion process. A prior resistivity of 100 m was chosen. Figures 32A and B show the inversion results of TDEM synthetic data calculated at flight altitudes of 90 m and 140 m for 100 model samples. Inversion results for 140 m altitude indicate that inverted TDEM data are able to recover the true model with a good approximation at a depth of more than 30 m.

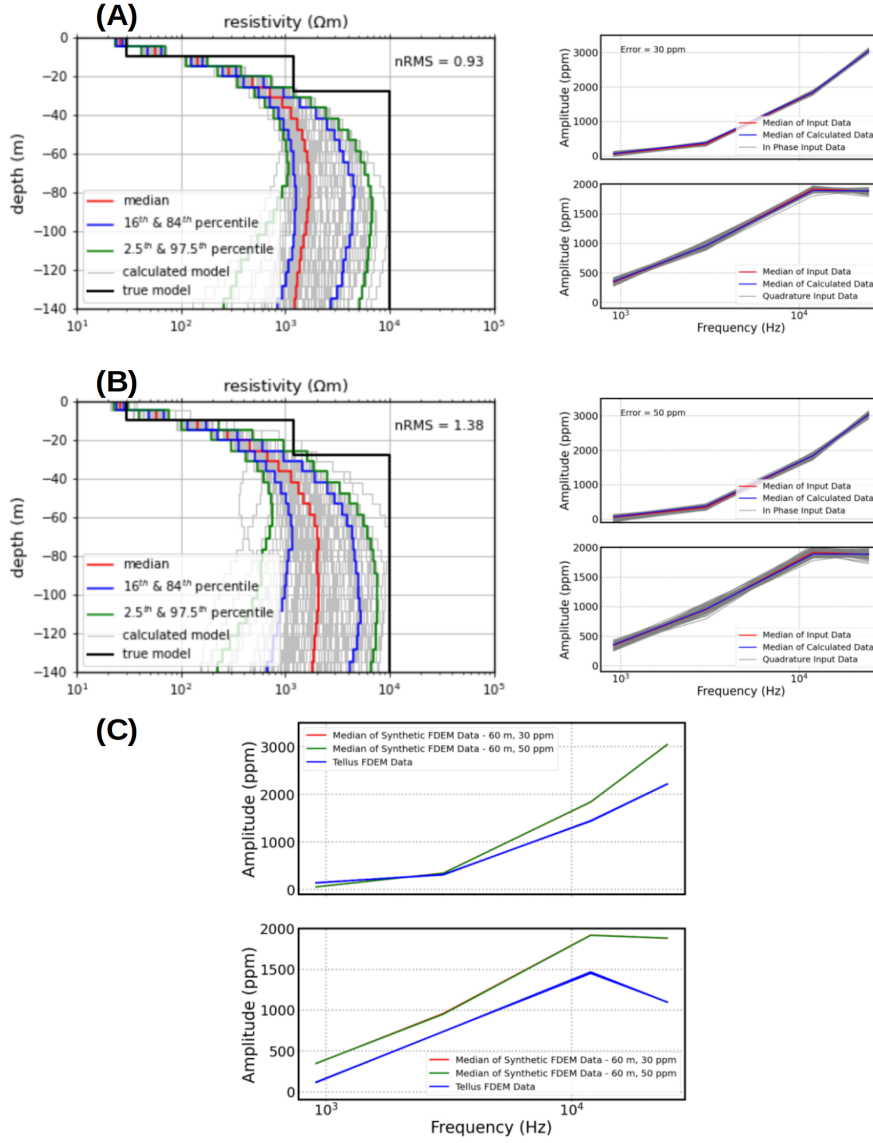


Figure 31: 1-D Tikhonov-type inversion results of FDEM synthetic data for a three-layer model simulated based on the simplified ERT resistivity model (Fig. 30) at the flight altitude of 60 m for 100 model samples. Data error assumptions were (A) 30 ppm and (B) 50 ppm. The plots on the left-hand side show the true model with the solid black line and the resistivity value of each 100 model sample is shown with the light solid grey lines, and the median resistivity value of 100 model samples is shown with the solid red line. The bounds that contain 68 and 98 percent of 100 model samples are shown with the blue and green solid lines, respectively. The right-hand side panel illustrates the data fit. The forward responses (i.e., input data) of 100 model samples are represented with the dark grey solid lines and the median of the input data is represented with the red solid line. The median of the predicted data is represented with the blue solid line. The regularisation parameters,  $\tau_0 = 0.01$  and  $\tau_1 = 0.1-100$  were chosen. (C) Observed Tellus FDEM data at one single site coincident with electrode number 22 of the ERT profile with the forward responses of the ERT-derived resistivity model simulated using a flight altitude of 60 m.

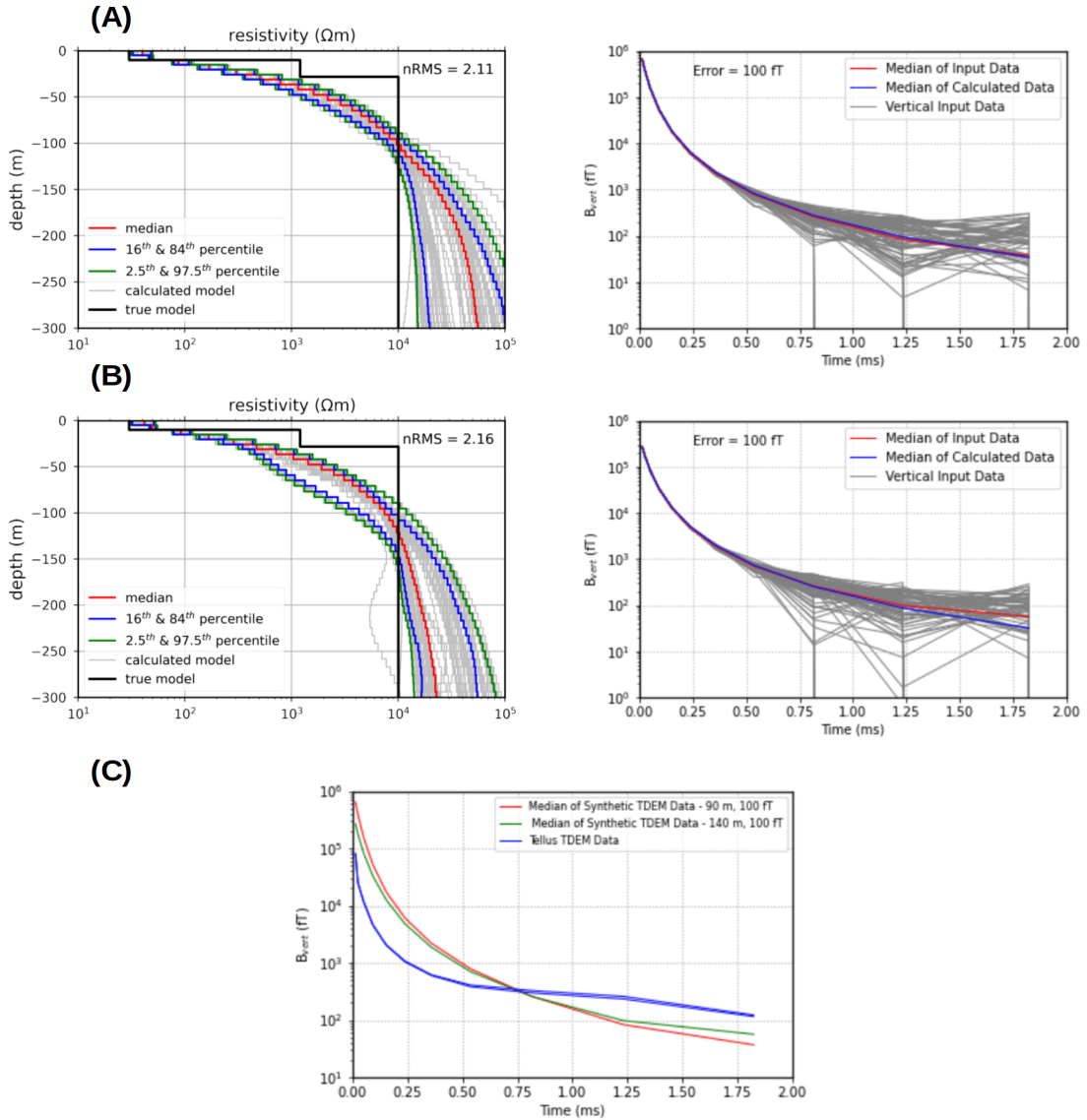


Figure 32: 1-D Tikhonov-type inversion results of TDEM synthetic data for a three-layer model simulated based on the simplified ERT resistivity model (Fig. 30) at the flight altitudes of (A) 90 m and (B) 140 m, for 100 model samples. The plots on the left-hand side show the true model with the solid black line and the resistivity value of each 100 model sample is shown with the light solid grey lines and the median resistivity value of 100 model samples with the solid red line. The bounds that contain 68 and 98 percent of the 100 model samples are shown with the blue and green solid lines, respectively. The right-hand side panel illustrates the data fit. The forward responses (i.e., input data) of 100 model samples are represented with the dark grey solid lines and the median of the input data is represented with the red solid line. The median of the predicted data is represented with the blue solid line. The regularisation parameters,  $\tau_0 = 0.01$  and  $\tau_1 = 0.1-100$  were chosen. (C) Observed Tellus TDEM data at one single site coincident with electrode number 22 of the ERT profile with the forward responses of the ERT-derived resistivity model simulated using a flight altitudes of 90 m and 140 m.

## 6 Conclusions

The ability to rapidly acquire airborne electromagnetic (AEM) data over relatively large survey areas makes this type of data an attractive tool for assessing changes in subsurface properties. Publicly available Tellus AEM data have brought an unprecedented opportunity to go beyond the current state-of-the-art by assessing the resolution, precision, and reliability of the subsurface resistivity models derived from these data. Additionally, the availability of co-located data acquired using frequency-domain (FDEM) and time-domain (TDEM) airborne systems makes it possible to carry out a thorough study on the uncertainty and resolution analysis of derived resistivity models. With the aim of carrying out a comparison between the two types of AEM data, synthetic data were simulated using two simple three-layer earth models. The shallow model comprises 15 m thick first layer with a resistivity of 100  $\Omega\text{m}$ , 25 m thick middle layer with a resistivity of 5  $\Omega\text{m}$ , and a lower half-space with a resistivity of 100  $\Omega\text{m}$ , respectively. The deep model comprises 50 m thick first layer with a resistivity of 100  $\Omega\text{m}$ , 50 m thick middle layer with a resistivity of 10  $\Omega\text{m}$ , and a lower half-space with a resistivity of 100  $\Omega\text{m}$ . The forward and inverse modelling of the synthetic data were carried out using aempy(x) toolbox written and developed by the Dublin Institute for Advanced Studies researchers. The 1-D inversion process has considered parameters including flight altitude, data errors, and input data, which can have significant effects on the resulting electrical conductivity models. The simulation results show that the FDEM data calculated at four Tellus survey frequencies at the flight altitudes of 60 – 120 m have done a much better job recovering the conductive middle layer of the shallow model. On the other hand, TDEM data calculated at eleven Tellus survey time channels have successfully recovered the first two layers of the second deep model even at the high flight altitudes of 100, 120, and 150 m. Due to the negative values observed in the in-line component of the TDEM data, inversions were carried out with the vertical component only.

As part of this study, an Electrical Resistivity Tomography (ERT) survey was carried out in September 2022 in an overlap zone, where both FDEM and TDEM data are available. Comparison of ERT and TDEM-derived models shows a good agreement at greater depths, however, the resolution of the ERT data was noticeably higher in the shallower subsurface, particularly where a thin conductive layer ( $< 30 \Omega\text{m}$ ) occurred within the 10 m. The Tellus FDEM data successfully resolved the conductivity of the top layer only, which is in good agreement with the ERT model.

## Bibliography

- [1] Fountain, D. (1998). Airborne electromagnetic systems – 50 years of development: Exploration Geophysics, 29, 1-11.
  - [2] Legault, J. M. (2015). Airborne electromagnetic systems - state of the art and 697 future directions, CSEG Recorder 40, 38-49.
  - [3] Kiyan, D.; Rath, V.; Mark R, M.; Ture, M.; Hodgson, J. (2022). 1-D inversion of frequency-domain airborne electromagnetic data using the open-source aempy toolbox, Journal of Applied Geophysics.
  - [4] Maxwell, J. C. (1892). A treatise on electricity and magnetism,Clarendon Press.An unabridged, slightly altered, republication of the two third edition volumes bound as one: Dover Publications, 1954. .
  - [5] Grant, I. S.; Phillips, W. R. (1990). Electromagnetism,John Wiley Sons, 137-221, 2ndedn.
  - [6] Brodie, R. C. (2017). Holistic Inversion of Airborne Electromagnetic Data Research School of Earth Sciences, Australian National University, PhD thesis.
  - [7] Zhdanov, M.; Keller, G. (1994). The geoelectrical methods in geophysical exploration . Methods in Geochemistry and Geophysics, 31, Elsevier.
  - [8] Niu, Q.; Prasad, P. (2016). Measurement of dielectric properties (mHz - MHz) of sedimentary rocks, SEG International Exposition and 86th Annual Meeting.
  - [9] Keller, G. (1988). Rock and mineral properties, in Nabighian, M.N. ed., Electromagnetic methods in applied geophysics, Volume 1, Theory; Investigations in Geophysics No. 3, Society of Exploration Geophysicists, 13-51.
  - [10] Palacky, G. (1993). Use of airborne electromagnetic methods for resource mapping, Advances in Space Research, 13, no. 11, 5-13.
  - [11] Palacky, G. J.; West, G. F. (1991). Airborne electromagnetic methods, in Nabighian,M.N. ed., Electromagnetic methods in applied geophysics,2, Application, Parts A and B; Investigations in Geophysics No. 3: Society of Exploration Geophysicists, 811-879.
  - [12] Dentith, M.; Mudge, S. (2014). Geophysics for the mineral exploration geoscientist. Cambridge University Press.
  - [13] Sengpiel, K. P. (1983). Resistivity/depth mapping with airborne eletromagnetic survey data: Geophysics, 48, no. 2,in Nabighian,M.N. ed., Electromagnetic methods in applied geophysics, 181-196.
  - [14] Fitterman, D. V.; Deszcz-Pan, M. (1998). Helicopter EM mapping of saltwater intrusion in Everglades National Park, Florida:Exploration Geophysics, 29, volume 12, 240-243.
  - [15] Sattel, D.; Kgolihang, L. (2004). Groundwater Exploration with AEM in the Boteti area, Botswana:Exploration Geophysics, 35, 147-156.
  - [16] Auken, E.; Westergaard, J.; Christiansen, A. V.; Sorensen, K. (2007). Processing and inversion of SkyTEM data for high resolution hydrogeophysical surveys: 19th International Geophysical Conference and Exhibition,Australian Society of Exploration Geophysicists, Extended Abstracts. .
-

## BIBLIOGRAPHY

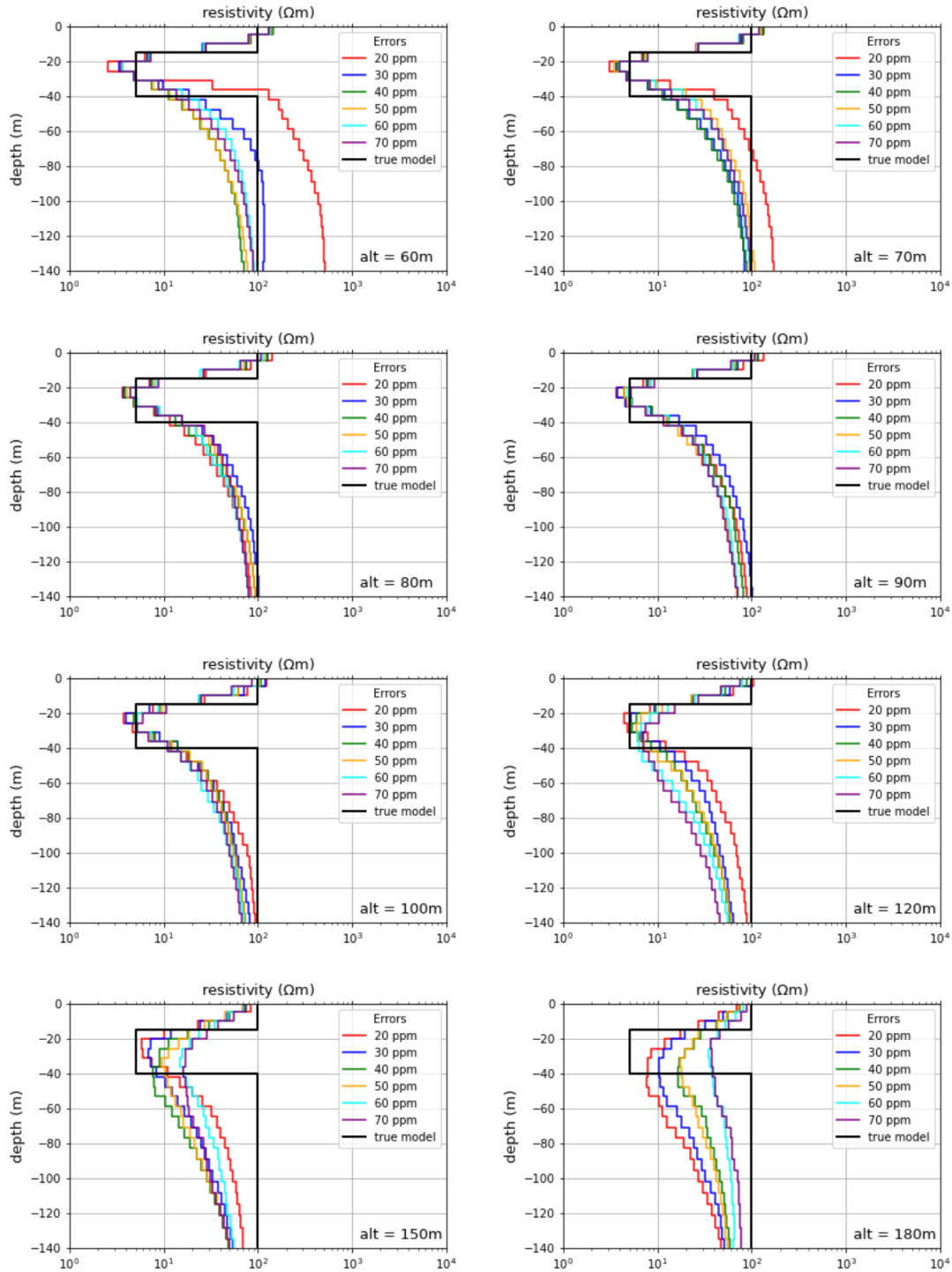
---

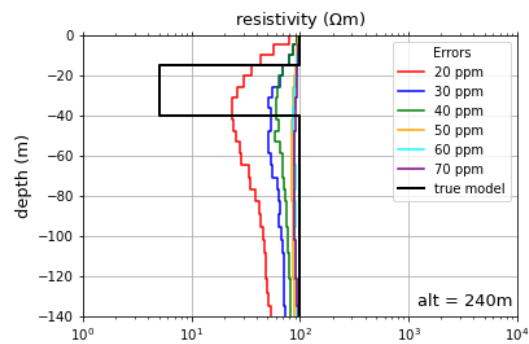
- [17] Anderson, H. A.; Duncan, A. C.; Lynch, S. M. (1993). Geological mapping capabilities of the QUESTEM airborne electromagnetic system for mineral exploration — Mt. Isa Inlier, Queensland: *Exploration Geophysics*, 24, 333–340.
- [18] Street, G. J.; Pracilio, G.; Nallan-Chakravartula, P.; Nash, C.; Sattel, D.; Owers, M.; Triggs, D. (1998). National Dryland Salinity Program Airborne geophysical surveys to assist planning for salinity control; 1. Willaura SALTMAP Survey Interpretation Report:National Airborne Geophysics Project, World Geoscience Corporation, Perth, WA.
- [19] Lawrie, K. C.; Munday, T. J.; Dent, D. L.; L.Gibson, D.; Brodie, R. C.; Wilford, J.; Reilly, N. S.; Chan, R. N.; Baker, P. (2000a). A geological systems approach to understanding the processes involved in land and water salinisation; the Gilmore project area, central-west New South Wales: AGSO Research Newsletter, 32, 13-15.
- [20] Lane, R.; Brodie, R. C.; Fitzpatrick, A. (2004b). A revised inversion model parameter formulation for fixed wing transmitter loop – towed bird receiver coil time-domain airborne electromagnetic data: 17th Geophysical Conference and Exhibition, Australian Society of Exploration Geophysicists, Extended Abstracts.
- [21] Klein, J.; Lajoie, J. J. (1980). Electromagnetic prospecting for minerals: In “Practical geophysics for the Exploration geologists”, edited by R. Van Blaricom, Northwest Mining Association, 239-290.
- [22] Kiyan, D.; Rath, V. (2017). Inverse Methods for Airborne Electromagnetic Data from the Tellus Surveys: The Aempty Toolbox, DIAS.
- [23] Allard, M. (2007). On the origin of HTEM species, In “Proceedings of Exploration 07: Fifth Decennial International Conference on Mineral Exploration” edited by B. Milkereit, 355-374.
- [24] Muller, M. R.; Hodgson, J. A. (2020). Tellus Waterford (WFD) Block: aempty Electromagnetic Inversion Report. Geological Survey Ireland Report.
- [25] Ture, M. D.; Hodgson, J.; Brady, A. (2017), Tellus GTK-FDEM system characteristics and applications, Geological Survey Ireland Report.
- [26] Hodgson, J. A.; Young, M. E. (2017). The Tellus airborne geophysical surveys and results’ in M.E. Young (ed.), Unearthed: impacts of the Tellus surveys of the north of Ireland, Dublin, Royal Irish Academy.
- [27] Cole, K. S.; Cole, R. H. (1941). Dispersion and absorption in dielectrics- I alternating current characteristics, *J. Chem. Phys.*, 9, 341–352.
- [28] Reynolds, J. M. (2011). An Introduction to Applied and Environmental Geophysics, 2nd Edition. New York, NY: Wiley-Blackwell.

## Appendices

### A

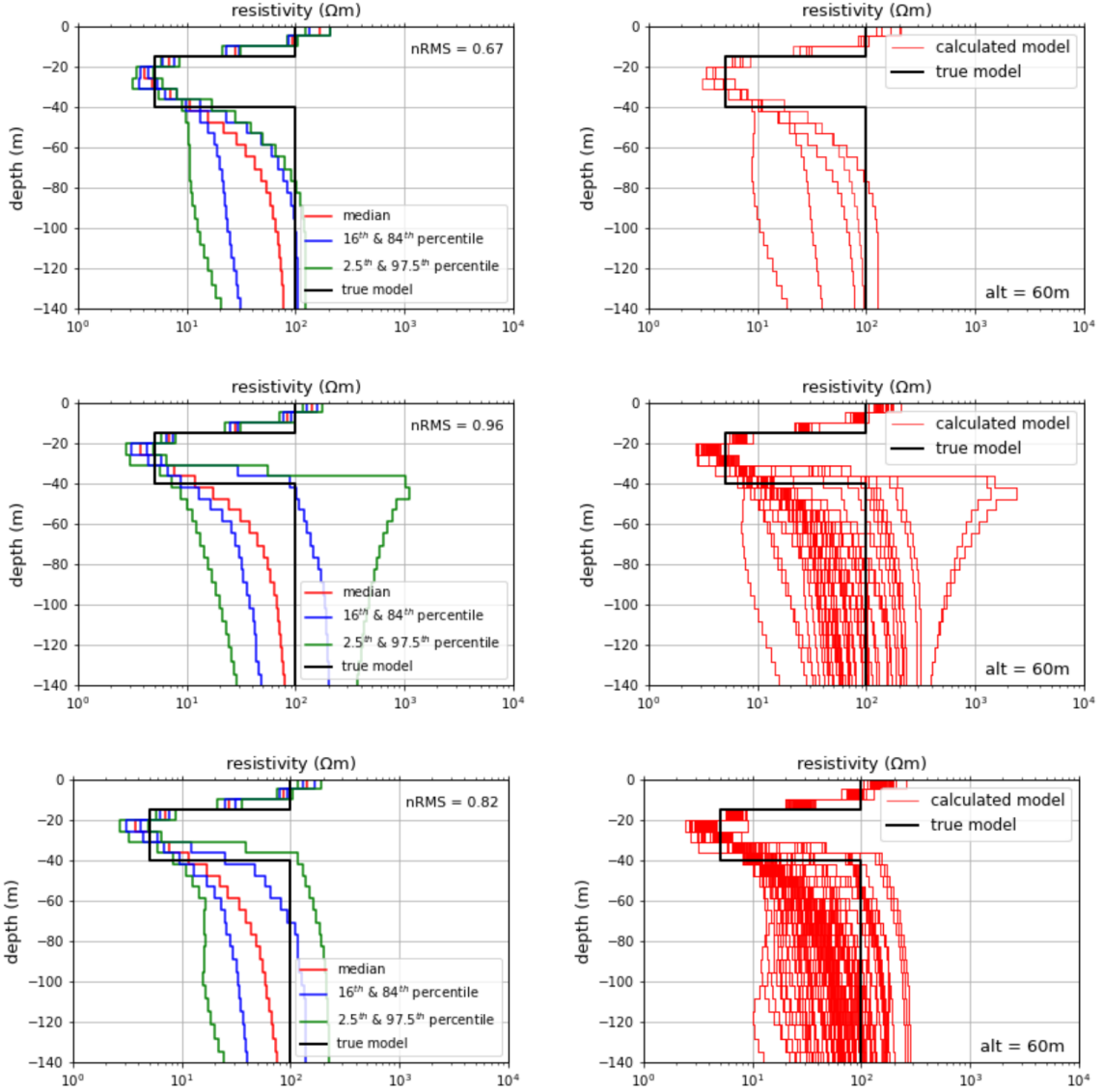
The following plots visualise the effect of different error assumptions on the inverted models for flight altitudes of 60 m, 70 m, 80 m, 90 m, 100 m, 120 m, 150 m, 180 m, and 240 m. Inversion regularisation parameters,  $\tau_0 = 0.01$  and  $\tau_1 = 0.1\text{-}20$  were chosen.





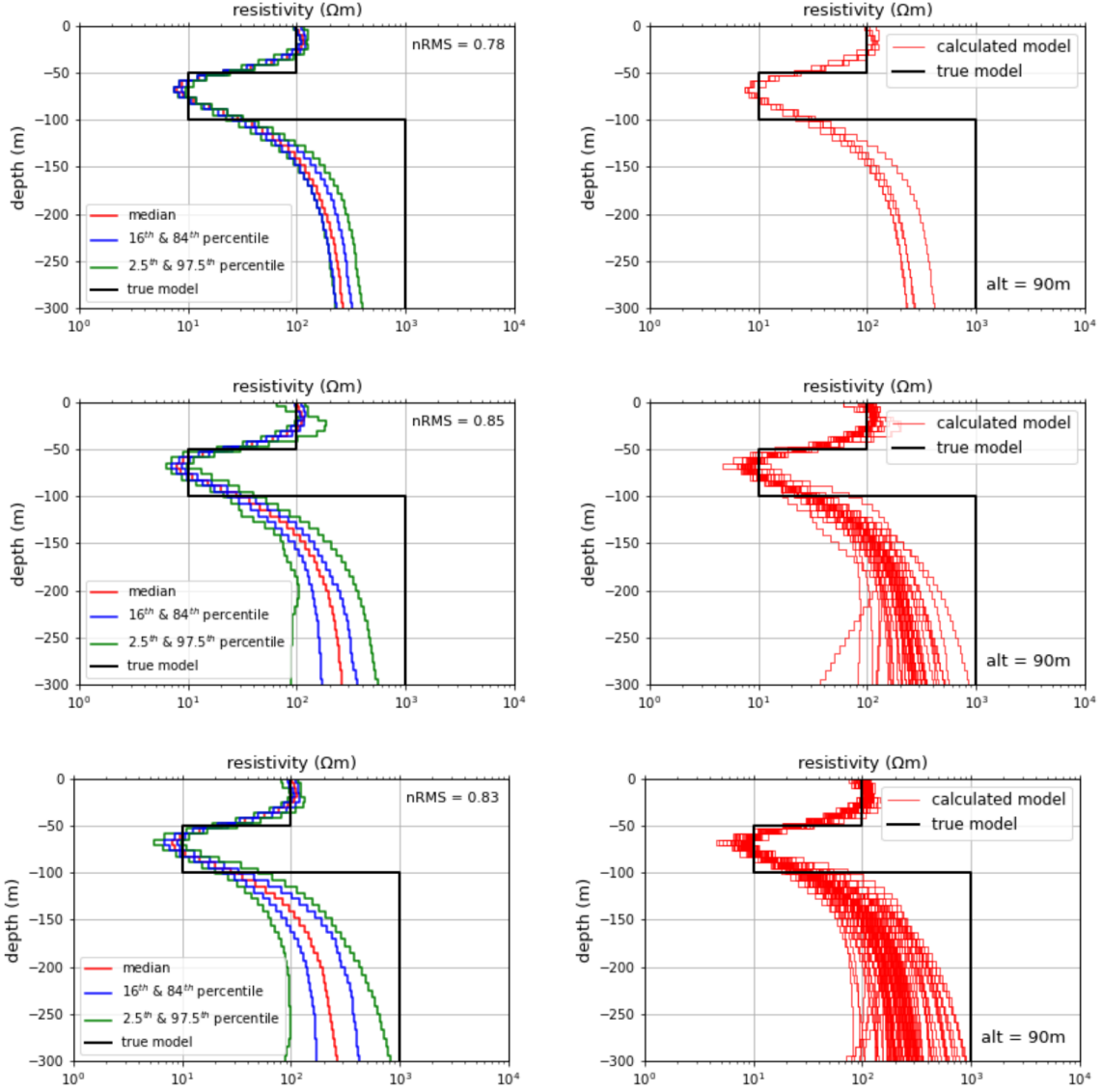
**B****B.1**

Tikhonov-type inversion results for a three-layer model at the flight altitude of 60 m for 5 model samples (top row), 50 model samples (middle row), and 100 model samples (bottom row) of FDEM synthetic data. The plots on the left-hand side show the true model with the solid black line and the median resistivity values of the model samples with the solid red line. The plots on the right-hand side show every single calculated model for 5, 50, and 100 samples. The data error assumption was 30 ppm and the regularisation parameters,  $\tau_0 = 0.01$ , and a range of  $\tau_1 = 0.1\text{-}100$  were chosen.



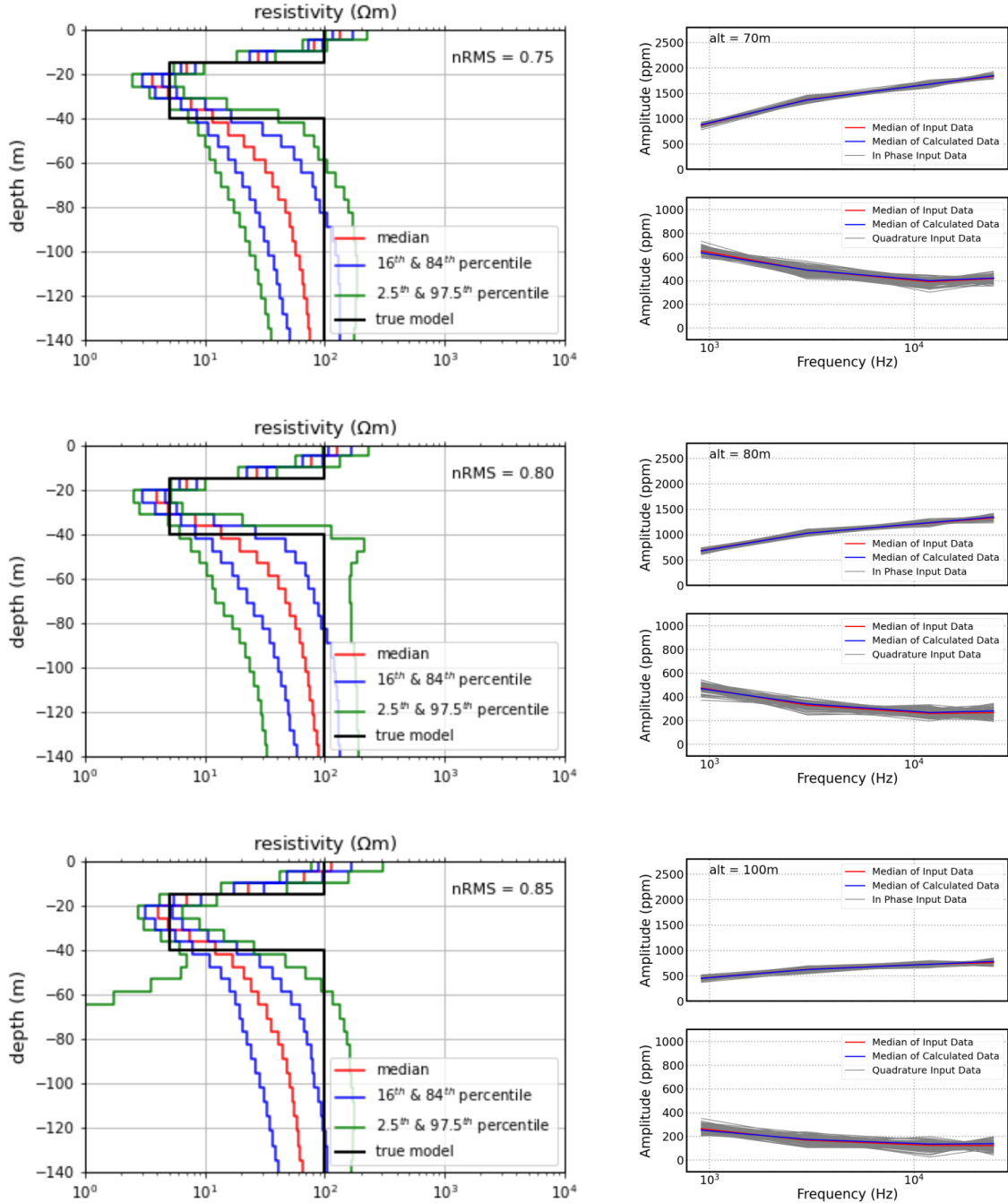
## B.2

Tikhonov-type inversion results for a three-layer model at the flight altitude of 90 m for 5 model samples (top row), 50 model samples (middle row), and 100 model samples (bottom row) of TDEM synthetic data. The plots on the left-hand side show the true model with the solid black line and the median resistivity values of the model samples with the solid red line. The plots on the right-hand side show every single calculated model for 5, 50, and 100 samples. The data error assumption was 3000 fT ppm and the regularisation parameters,  $\tau_0 = 0.01$ , and a range of  $\tau_1 = 0.1\text{-}100$  were chosen.



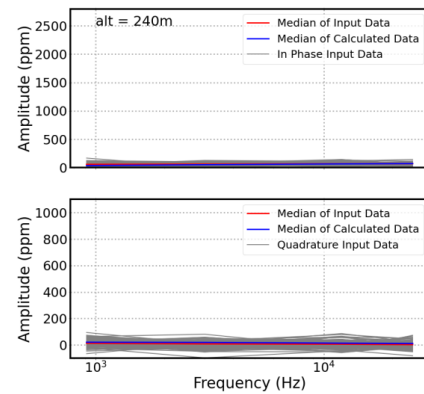
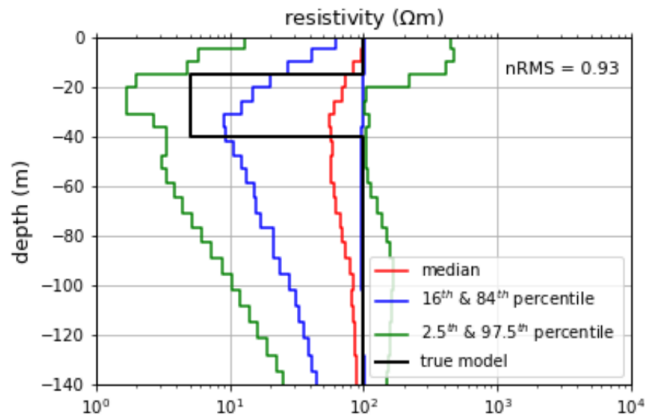
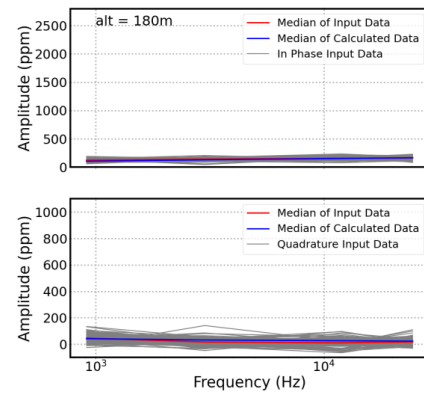
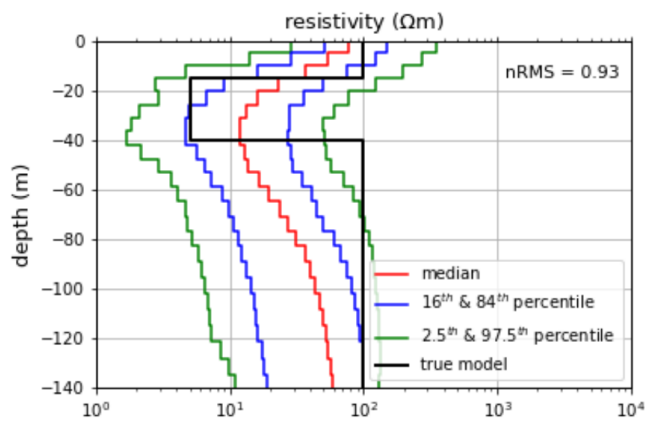
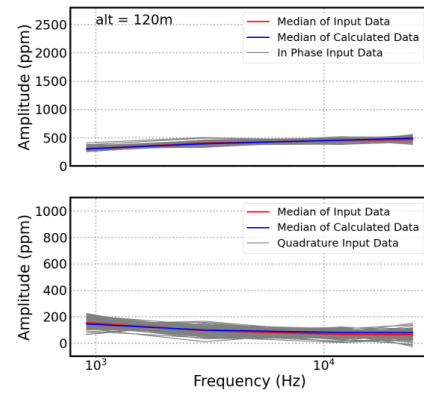
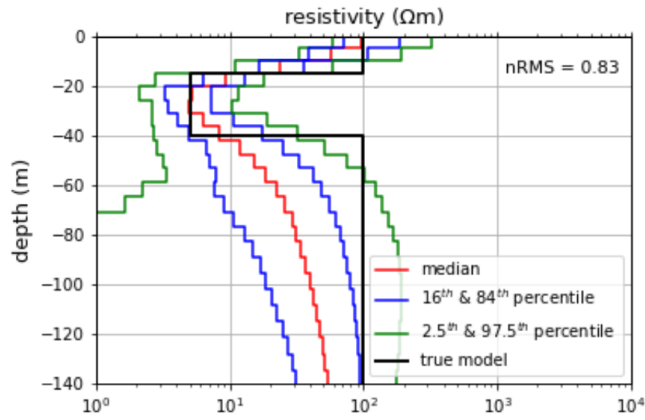
## C

Tikhonov-type inversion results for a three-layer model at the flight altitudes of 70 m, 80 m, 100 m, 120 m, 180 m, and 240 m for 100 model samples of FDEM synthetic data. Data error assumption 30 ppm, and the regularisation parameters,  $\tau_0 = 0.01$ , and a range of  $\tau_1 = 0.1\text{--}100$  were chosen.



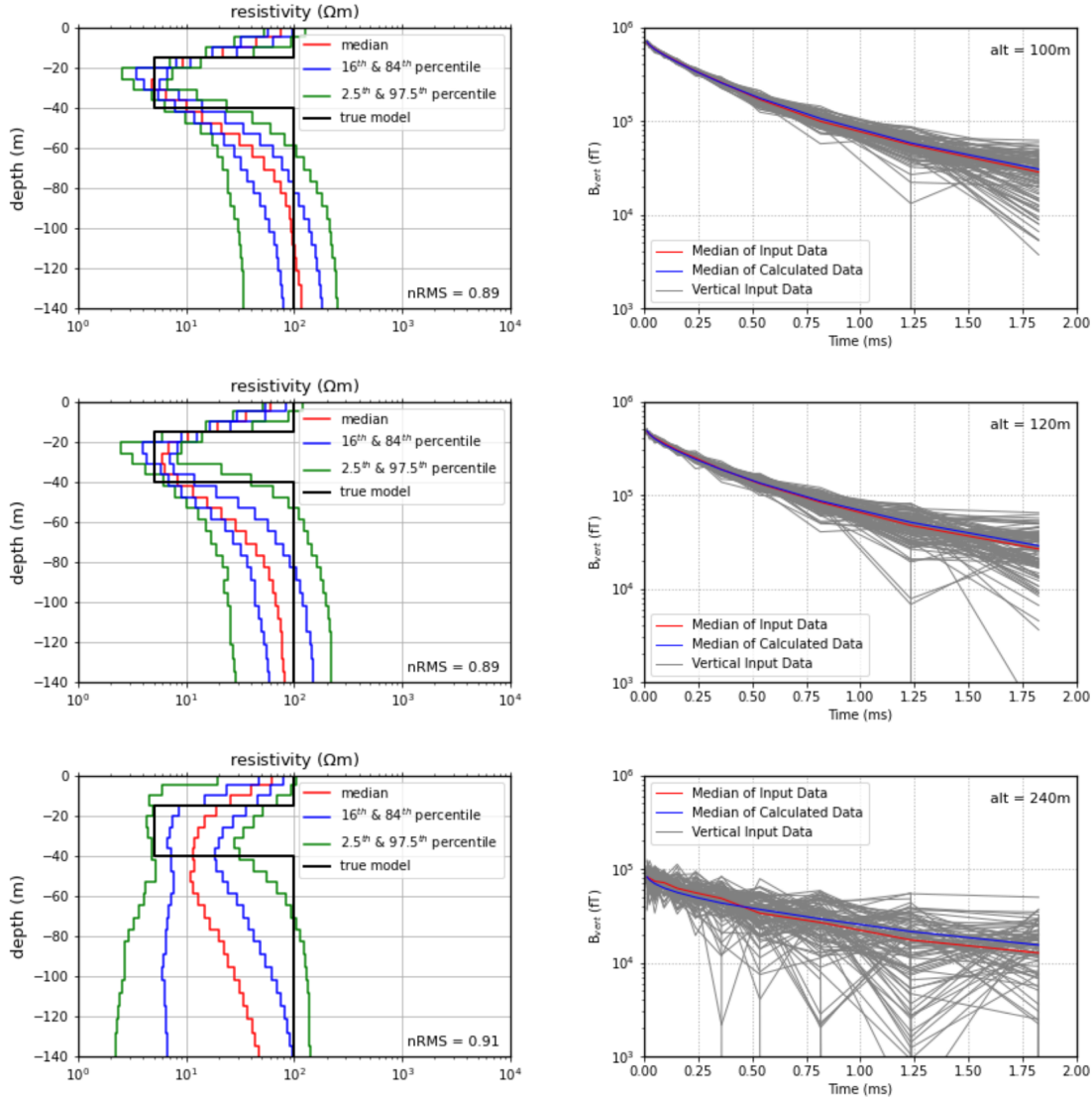
## APPENDICES

---



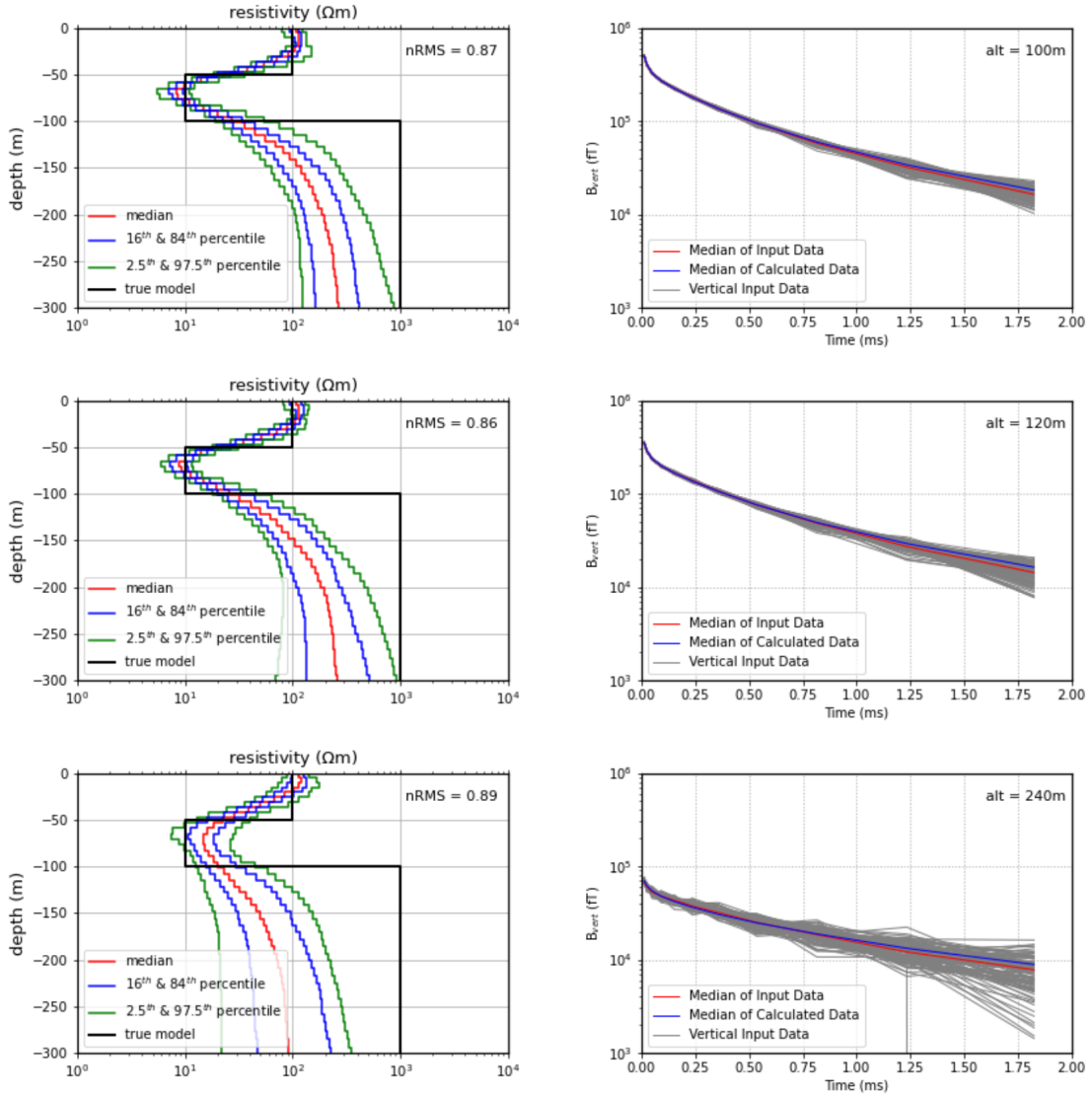
## D

Tikhonov-type inversion results for a three-layer model at the flight altitudes of 100 m, 120 m, and 240 m for 100 model samples of TDEM synthetic data. The data error assumption was 15000 fT and the regularisation parameters,  $\tau_0 = 0.01$ , and a range of  $\tau_1 = 0.1\text{--}100$  were chosen.



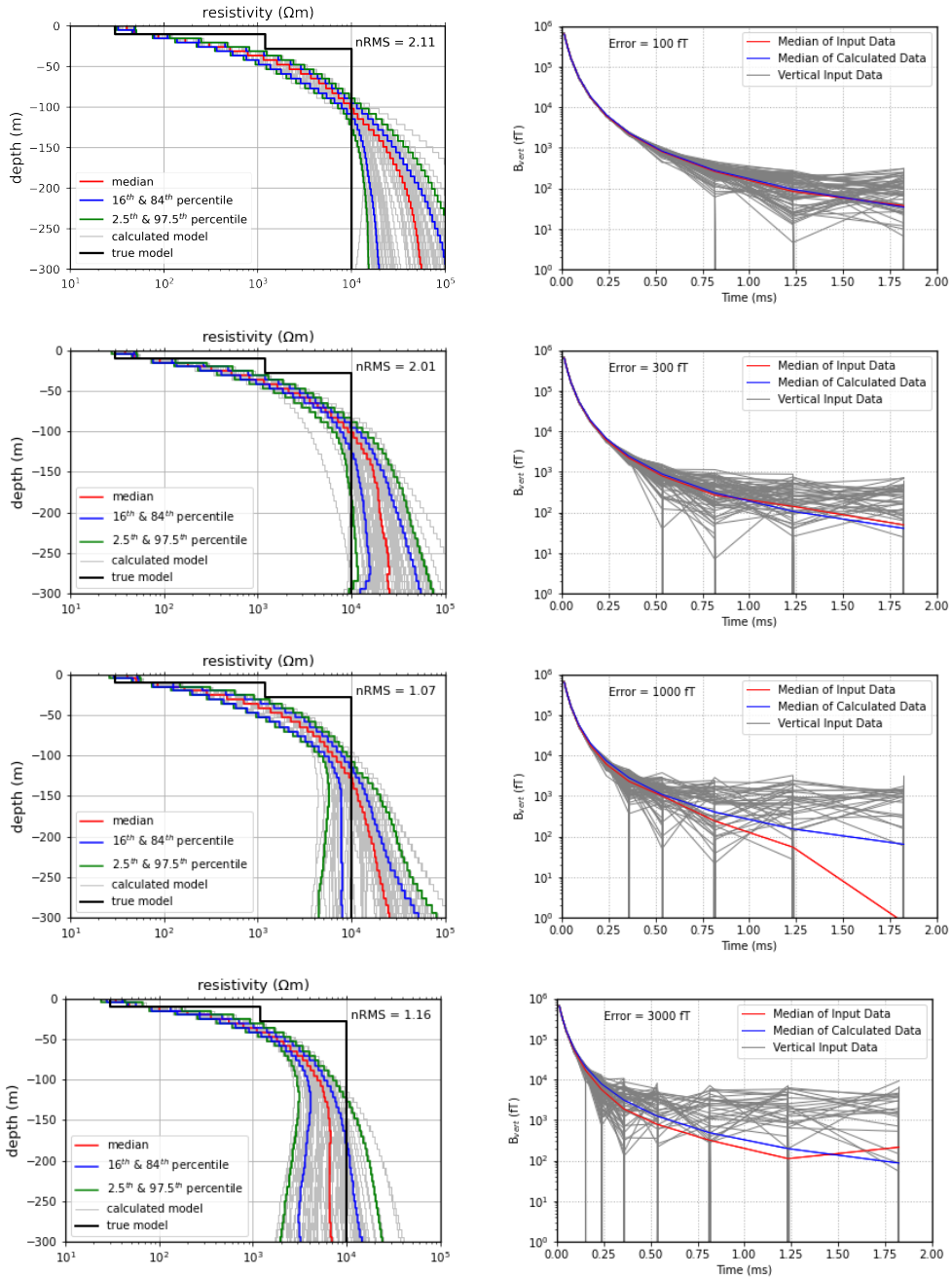
## E

Tikhonov-type inversion results for a three-layer model at the flight altitudes of 100 m, 120 m, and 240 m for 100 model samples of TDEM synthetic data. The data error assumption was 3000 fT and the regularisation parameters,  $\tau_0 = 0.01$ , and a range of  $\tau_1 = 0.1\text{-}100$  were chosen.



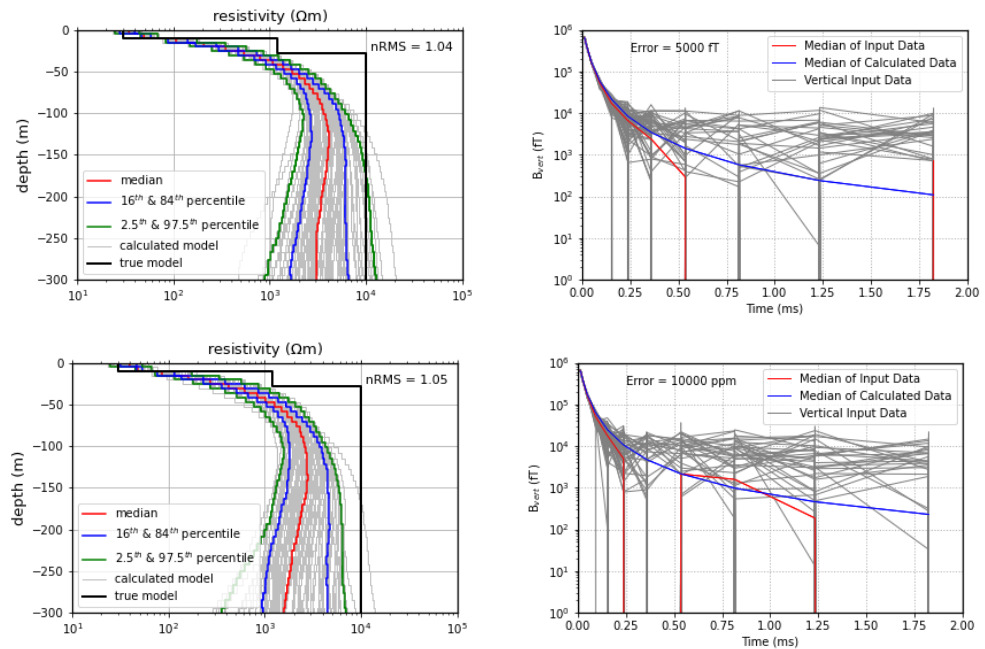
## F

Tikhonov-type inversion results of TDEM data for a three-layer model simulated based on the simplified ERT resistivity model (Fig. 30) at the flight altitude of 90 m, for 100 model samples with different data error assumptions. The plots on the left-hand side show the true model with the solid black line and the resistivity values of each 100 model samples shown in light solid grey lines, and the median resistivity values of 100 model samples with the solid red line. The bounds that contain 68 and 98 percent of the 100 model samples are shown with the blue and green solid lines, respectively. The right panel illustrates the data fit and median of the input and calculated data. 100 model samples are represented with dark grey solid lines and the median of the input data is represented with a red solid line. The median of predicted data is represented with the blue solid line. The regularization parameters,  $\tau_0 = 0.01$ , and a range of  $\tau_1 = 0.1\text{-}100$  were chosen.



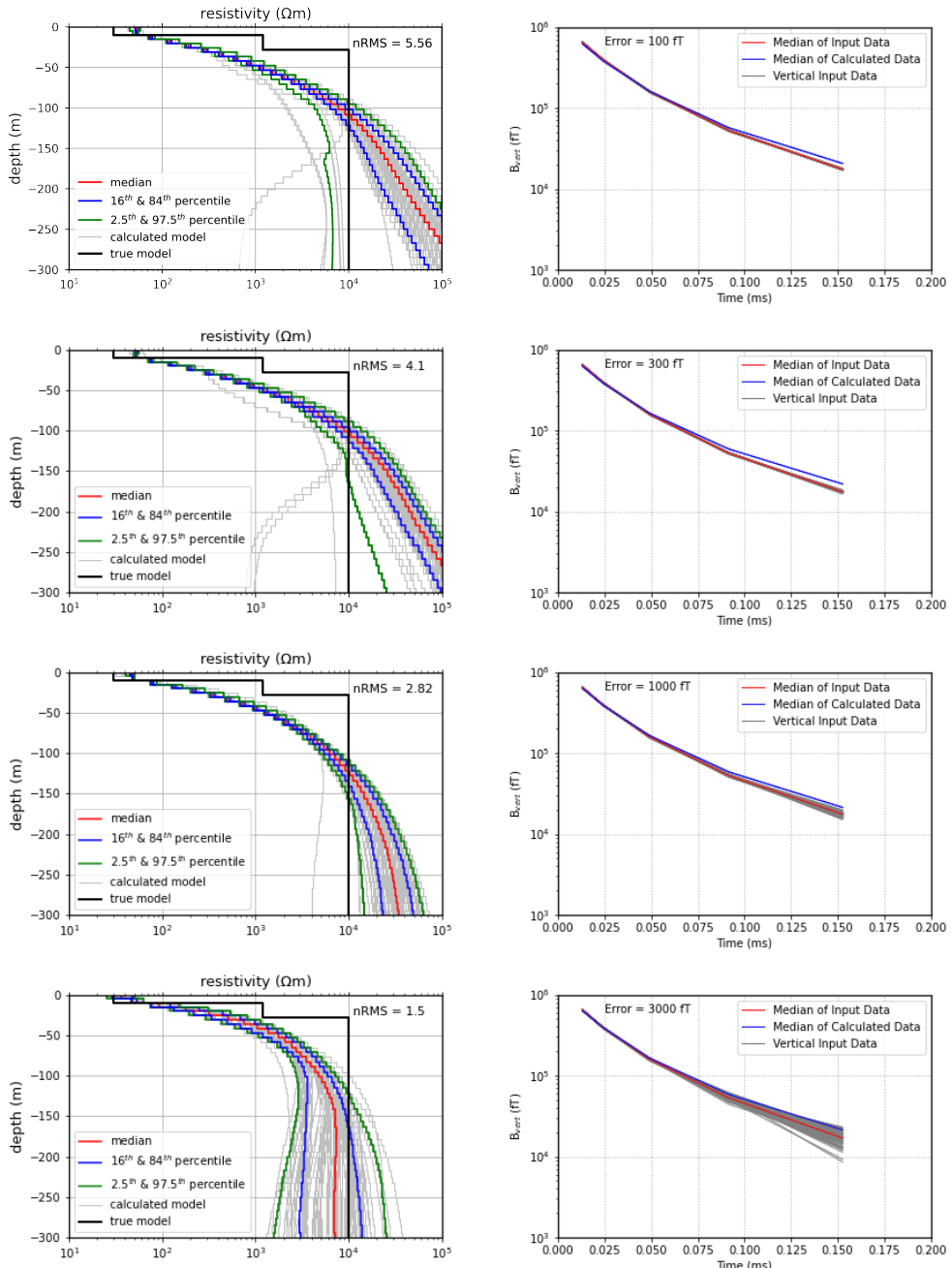
## APPENDICES

---



## G

Tikhonov-type inversion results for the first five Tellus time channels of TDEM data for a three-layer model simulated based on the simplified ERT resistivity model (Fig. 30) at the flight altitude of 90 m, for 100 model samples with different data error assumptions. The plots on the left-hand side show the true model with the solid black line and the resistivity values of each 100 model samples shown in light solid grey lines, and the median resistivity values of 100 model samples with the solid red line. The bounds that contain 68 and 98 percent of the 100 model samples are shown with the blue and green solid lines, respectively. The right panel illustrates the data fit and median of the input and calculated data. 100 model samples are represented with dark grey solid lines and the median of the input data is represented with a red solid line. The median of predicted data is represented with the blue solid line. regularisation parameters,  $\tau_0 = 0.01$ , and a range of  $\tau_1 = 0.1\text{-}100$  were chosen.



## APPENDICES

---

